Articles in PresS. J Neurophysiol (April 25, 2012). doi:10.1152/jn.00098.2011

# Pitfalls in the dipolar model for the neocortical EEG sources

[1]*Riera JJ,* [†1]*Ogawa T,* [†1]*Goto T,* [1]*Sumiyoshi A,* [1]*Nonaka H,* [2]*Evans A,* [3]*Miyakawa H,* [1]*Kawashima R*

[1]Institute of Development, Aging and Cancer (IDAC), Tohoku University, Sendai; [2]McConnell Brain Imaging Centre, Montréal Neurological Institute, McGill University, Montréal; [3]School of Life Sciences, Tokyo University of Pharmacy and Life Sciences, Tokyo

*Running title:* Pitfalls in the EEG dipolar model

*†- Authors contribute equally*

*Correspondence to:* Jorge J. Riera

Associate Professor, PhD in Physics
Department of Functional Brain Imaging
Institute for Development, Aging and Cancer
Tohoku University
4-1 Seiryocho, Aobaku, Sendai 980-8575, JAPAN
TEL/FAX:
+81-22-717-8468 (Lab)
+81-22-717-8466 (Office)
email: riera@idac.tohoku.ac.jp

# Abstract

For about six decades, primary current sources of the electroencephalogram (EEG) have been assumed dipolar in nature. In this study, we used electrophysiological recordings from anesthetized Wistar rats undergoing repeated whisker deflections to revise the biophysical foundations of the EEG dipolar model. In a first experiment, we performed three-dimensional recordings of extracellular potentials from a large portion of the barrel field to estimate intra-cortical multipolar moments generated either by single spiking neurons (i.e. pyramidal cell, PC; spiny stellate cells, SS) or by populations of them while experiencing synchronized postsynaptic potentials. As expected, back-propagating spikes along PC dendrites caused dipolar field components larger in the direction perpendicular to the cortical surface (49.7±22.0 *nA mm*). In agreement with the fact that SSs have 'close-field' configurations, their dipolar moment at any direction was negligible. Surprisingly, monopolar field components were detectable both at the level of single units (i.e. –11.7±3.4 *nA* for PC) and at the mesoscopic level of mixed neuronal populations receiving extended synaptic inputs within either a cortical column (–0.44±0.20 $\mu A$) or a 2.5 $m^3$-voxel volume (–3.32±1.20 $\mu A$). In order to evaluate the relationship between the macroscopically-defined EEG equivalent dipole and the mesoscopic intra-cortical multipolar moments, we performed concurrent recordings of high-resolution skull EEG and laminar local field potentials. From this second experiment, we estimated the time-varying EEG equivalent dipole for the entire barrel field using either a multiple dipole fitting or a distributed type of EEG inverse solution. We demonstrated that mesoscopic multipolar components are altogether absorbed by any equivalent dipole in both types of inverse solutions. We conclude that the primary current sources of the EEG in the neocortex of rodents are not precisely represented by a single equivalent dipole and that the existence of monopolar components must be also considered at the mesoscopic level.


**Abbreviations:** EEG/MEG, electro/magneto-encephalogram; CSD, current source density; LFP, local field potential; LORETA, low resolution electromagnetic tomography; aCSF, artificial cerebral spinal fluid; PC, pyramidal cells; SS, spiny stellate cells


**Keywords:** *EEG, neocortex, multipolar current sources, inverse problem*

# I. Introduction

The dipolar model, used by generations of neuroscientists to represent the current sources of the electroencephalogram (EEG) in humans (Walter and Walter 1949; Plonsey 1969; Niedermeyer and Lopes da Silva 1987; Nunez and Srinivansan 2006), has roots in early interpretations by Adrian and Matthews (1934) about the origin of the Berger rhythm (i.e. the alpha rhythm). These authors suggested that the cortical electric potentials formerly observed by Berger (1929) were caused by electrical sources close to the brain surface with a polarity inversion in the axis perpendicular to it. The existence of dipole-like field distributions with axes parallel to the cortical surface was later suggested by Beevers (1944), with confirmations for the kappa rhythm (Kennedy et al. 1948) and the epileptic focal seizures (Gumnit and Takahashi 1965). This model, which eventually gained popularities in many other emerging applications of EEG (e.g. *sleep*: Brazier 1949 and *epilepsy*: Gumnit and Takahashi 1965), was originally formulated by Shaw and Roth (1955) in terms of the electric field theory. The feasibility of estimating such dipolar sources from actual EEG data was successfully tested in several preliminary experiments (Henderson et al. 1975). Then, this methodology became one of the most remarkable breakthroughs in the EEG renaissance period that started with the substitution of polygraphs (i.e. ink-writing amplifiers) and cathode-ray oscilloscopes by the digital EEG amplifiers in the 80s, a situation that happened to occur almost at the same time that personal computers smashed IBM punch cards. In particular, parametric source analysis methods based on least-squares estimation of moving (Schneider 1972) and spatiotemporal (Scherg and VonCramon 1985) dipole models were at that time, and even are now (Mosher et al. 1992; Xu et al. 2004), very helpful to localize current sources inside the brain and to segregate them in circumstances of simultaneously activate regions. Furthermore, the concept of current dipole density underlies most of the modern imaging methods (Baillet et al. 2001), e.g. beamforming/MUSIC approaches and distributed source models. With the development of chronically implanted electrodes in humans during the 50s to treat psychiatric patients through a frontal leucotomy (Sem-Jacobsen et al. 1955) and also to characterize epileptic seizures (Abraham and Ajmone-Marsan 1958), it was possible to examine in situ the biophysical foundations of the EEG

dipolar model. During this early period, further comparative evaluations were also possible by the help of animal models.

For the cerebral cortex, researchers first focused on clarifying the strength and extension of the actual current dipoles. In a pioneer work, Cooper et al. (1965) concluded that a synchronous activation of a cortical area of 6 $cm^2$ is required to produce observable signal in the human EEG data, although subsequent studies showed that a recruitment of larger areas might be necessary (Ebersole 1997, 2000; Tao et al. 2005). More contemporary studies using simultaneous magnetoencephalographic (MEG) and subdural EEG recordings revealed that just an area of about 4 $cm^2$ of synchronized cortical activity is necessary to produce an observable MEG signal (e.g. *α rhythm* - Chapman et al. 1984; *epileptogenic activity* - Mikuni et al. 1997; Oishi et al. 2002). The first estimation of the cortical current density is attributable to bipolar recordings from the prepyriform cortex of adult anesthetized cats (Freeman 1959), which clearly showed the existence of voltage differences of up to 1.5 *mV* between electrodes that were 1.5 *mm* apart. Note that in this preliminary study the position of the electrodes were inserted perpendicular to the cortical surface until a maximal dipolar-field configuration was evoked by electrical stimulation of the olfactory bulb. A second estimation emanated from extracellular potentials of spike-wave responses in the precruciate cortex in cats that were evoked by stimulation of the thalamus (Pollen 1969). This author found voltage gradient along the cortical laminas of up to 400-450 *μV/mm*. Taking into account these observations and timely estimations of the cortical conductivity (e.g. *rabbits*: 2.73–3.62 *mS/cm*, Ranck 1963; *cats*: 1.66–1.96 *mS/cm*, Li et al. 1968), it was possible through the use of the methodology proposed by Humphrey (1968) to obtain ranges (100–250 $nA/mm^2$) for the typical transcortical current densities (Pollen 1969; Freeman 1975), which remain valid until these days (Baillet et al. 2001). The strengths and spatial extensions of cortical dipoles were in agreements with estimations obtained from EEG and MEG data (10-100 *nA-m*, Cohen and Cuffin 1983; Chapman et al. 1984; Bowyer et al. 1999; Jones et al. 2007, 2009). Additionally, these values were compatible with later predictions of the transcortical current density from anatomo-physiological considerations (Hämäläinen and Ilmoniemi 1984; Hari and Ilmoniemi 1986; Hämäläinen et al. 1993).

Understanding the laminar/neuronal substrates of the actual cortical dipoles constituted a second issue of interest in the past. In fact, the existence of cortical dipoles was initially supported by the observation of phase reversals between an electrode lying on the cortical surface and other in the white matter beneath the cerebral cortex (Calvet and Scherrer 1961). Later, Lopes da Silva and van Leeuwen (1977) provided convincing evidence for a phase reversal (i.e. $180^{o}$ about 1100 $\mu m$ from the cortical surface) in the case of alpha rhythm recordings from unrestrained dogs. Such observations were consistent with studies that explained the spontaneous EEG by the succession/mingling of the activities of different types of dipoles distributed along the cortical layers (*cats* - Calvet et al. 1964, *rabbits* - Rappelsberger et al. 1982), with the PCs at both the infra and supra –granular layers being the most important contributors (Kraut et al. 1985; Di et al. 1990). Even so, other studies claimed that the concept of phase reversal was only valid to a limited extent (Gumnit and Takahashi 1964; Petsche et al. 1977). In particular, it was pointed out that true mirror images are hardly observed in practice, and when they were, the temporal coherence estimates between the corresponding sources and sinks were very low. In many contemporary studies, current source density (CSD) distributions inside the neocortex have been examined with much better accuracy by the help of both high-resolution silicon-based microelectrodes arrays and advanced mathematical constructs. Indeed, the existence of unbalanced currents sources with no clear reversals in the laminar polarity is also suggested from CSD distributions in the somatosensory (Di et al. 1990; Ahrens and Kleinfeld 2004; Higley and Contreras 2007; Mégevand et al. 2008), motor (Ahrens and Kleinfeld 2004), visual (Lakatos et al. 2008) and auditory (Lakatos et al. 2007) cortices for a variety of experimental paradigms. As an alternative explanation for these unbalanced-CSD distributions, some researchers have presupposed that additional current source/sink distributions with counterpart polarity might exist along the tangential directions to the cortical surface (e.g. Nunez P, personal communication). Likewise, even though shifted-dipoles were initially associated with back-propagating action potentials in layer V PCs (Buzsáki and Kandel 1998), exact balanced-CSD patterns are not that evident from estimation with highest spatial resolutions (Bereshpolova et al. 2007).

Lastly, biophysical models of single neurons were used from the beginning to establish the neuronal foundations of the extracellular potentials and hence of the EEG data. For instance, based on the extracellular potentials generated by an axon undergoing an action potential, Lorente de Nó (1947) proposed the concept of 'open' and 'closed' field configurations for remote EEG observations. In this initial work, the extracellular potentials were calculated by approximating each cell by point sources with strengths determined by the electric currents flowing across the corresponding cell membrane patches. Succeeding theoretical studies determined the extracellular electric potentials generated by synaptic inputs to the somas of either single neurons (Rall 1962) or populations of them (Klee and Rall 1977). As a result of having the dendrites organized along a particular direction, PCs have been classified as open field neurons. In contrast, as a consequence of their radially symmetric dendrites, spiny stellate (SS) cells are thought to have a closed field configurations. These previous studies are based on the quasi-static approach of the electric fields in the brain tissues (Plonsey and Heppner 1967) and the compartmental models of neurons (Rall 1962; Johnston and Wu 1994). Original compartmental models of neurons resulted from: **a)** the introduction of dimensionless distance/time variables in the cable equation, **b)** the linearization of ionic current kinetics inside each dendritic branch and **c)** the use of the equivalent cylinder theorem for dendritic trees (*i.e. determining input resistances for branches and dendritic attenuation effects*). The latter has been formulated on the basis of three main conditions: 1- the cumulative electrotonic length condition, 2- the 3/2 power law at every branch point condition and 3- the termination condition. Holt and Koch (1999) proposed more recently the line source model, which simplifies the dendrites by lines with zero widths. The cable equation constitutes the standard biophysical model underlying these previous studies, which is based explicitly in the Kirchhoff's current law. Therefore, the total current flowing across the whole cell membrane must be zero at each time instant, and as a consequence there will be no unbalanced currents sources inside the brain at a microscopic level[*]. This assumption has led us to reject, since the very beginning, the existence of monopolar current source components in any mesoscopic volume inside the

[*]**Definitions**: **a**) *microscopic level* → from a membrane patch to a single neuron, **b**) *mesoscopic level* → from a anatomical micro-column to a group of functional columns, "e.g. the barrel field", and **c**) *macroscopic level* → from a single brain area to the entire head

neocortex (Llinás and Nicholson 1974; Nunez 1981). More contemporaneous biophysical models for the genesis of the extracellular potentials are also built based on equivalent assumptions and theoretical frameworks (Gold et al. 2006, 2007; Murakami and Okada 2006; Jones et al. 2007; Pettersen and Einevoll 2008). However, Bédard and Destexhe (2009) suggested recently that the existence of ionic diffusion effects across the cellular membranes, which may be larger than any ohmic effect. These authors claimed that ionic diffusion is responsible for the frequency dependence of the electric conductivity/permittivity and provided a new explanation for the 1/f noise scaling in the local field potentials (LFP). Dehghani et al. (2011) found that the significant differences in the scaling of the power spectral density for the EEG and MEG could be also explained by considering high-dispersive effects in the brain tissues.

In this paper, we recapitulate the concept of cortical dipolar model in the light of recent advances both in technologies for electrophysiological recordings and in methods for the analysis of cortical CSD. First, using a customized three-dimensional probe we recorded LFP and unit activity from the barrel cortex of Wistar rats undergoing both single and whole whisker stimulations at 1 *Hz*. We used a method recently introduced by Goto et al. (2012) to estimate the volumetric CSD associated with both back-propagating action potentials in individual cells and population synaptic activities evoked by the whisker deflections. In both cases, we found important dipolar and quadrupolar contributions but also the existence of unbalanced current sources in the neocortex. In order to verify the impact of such local current unbalance in the EEG, and of any higher order multipoles as well, we used multi-scale electrophysiological data recorded from Wistar rats. This multi-scale data consists of high-density skull EEG recordings concurrently observed with laminar LFP through a silicon-based probe implanted in the barrel field while multiple whiskers were deflected at two different frequencies (1 *Hz* and 3 *Hz*). In this case, the analysis of mesoscopic CSD was performed using the inverse CSD (iCSD) method (Pettersen et al. 2006), and the results were used to estimate the multipolar moments for each stimulus frequency in the recorded barrel region. The dynamics of the equivalent macroscopic dipole in the barrel cortex were estimated from both a least square dipolar fitting (Jones et al. 2007) and the surface low resolution electromagnetic tomography

(LORETA*) type of inverse solution (Riera et al. 2000). The mesoscopic multipolar moments were normalized, and then used, as known-loadings in a linear regression analysis, to predict the time courses of the estimated EEG dipole for the whole barrel field.

# II. Materials and Methods

The experiments were performed in agreement with the policies established by the "*Animal Care Committee*" at Tohoku University, Sendai, Japan.

**Animal preparation**

Thirteen Wistar rats (8 *weeks*, male) were anaesthetized with urethane (1.2 *g/Kg*). For each rat, the scalp was partially removed, leaving a large portion of the skull exposed. A craniotomy of 2 *mm* in diameter was made on the right primary barrel cortex (Riera et al., 2010a). Two screws, used as a reference and ground for the intracranial electric recordings, were attached to the skull around the right mastoid. HEPES-buffered and $Ca^{2+}$-free artificial cerebral spinal fluid (aCSF, 150 *mM* NaCl, 2.5 *mM* KCl, 1 *mM* $MgCl_2 \cdot 6H_2O$, 10 *mM* HEPES, 10 *mM* glucose, the pH was adjusted to 7.4 with tris-base) was applied to the exposed cortex, after which, a small patch of dura matter from the top of the observation site was carefully removed. We prepared the rats for two types of experiments: **a)** volumetric extracellular recordings and **b)** concurrent EEG and LFP recordings.

*a) Volumetric extracellular recordings (N=4)*: We designed a three-dimensional silicon-based probe (NeuroNexus Technologies, Fig. 1 A) to record LFP from 128 locations inside 2.02 $mm^3$ of cortical tissue. This probe consists of a regular and parallel array of four laminar probes with iridium-oxide microelectrodes (i.e. area 177 $\mu m^2$, inter-microelectrode intervals 200 $\mu m$, distance between shanks 400 $\mu m$), which were separated by a distance of 400 $\mu m$. This arrangement results in a 4 x 4 regular grid of shanks covering, after insertion, a total cortical area of 1.44 $mm^2$ (i.e. several barrels). The three-dimensional probe was perpendicularly inserted in the barrel cortex and the craniotomy filled with non-conductive paraffin oil (Nacalai tesque).

*The classical surface LORETA is also based on a dipolar representation of the cortical current sources

*b) Concurrent EEG and LFP recordings (N=9)*: A gel with conductivity value adjusted to simulate that of the actual rat's skull (0.13±0.08 mS/cm) was applied on the craniotomy. By means of a fine brush, we applied a thin layer of this conductive gel to the exposed skull with a twofold intention: to improve the conductance at the electrode/skull interface and to keep the bone from drying throughout the experiment. A home-made EEG mini-cap (Fig. 1 B, top) was set on the rat's head by firmly attaching fixed-aluminum bars (one on the nasal channel and two posterior to the interaural line) to the skull using self-etching adhesive resin cement (Tokuyama Dental). Details about the EEG mini-cap as well as a method to achieve low electrode impedances are provided in Riera et al. (2010b). A similar EEG mini-cap was used recently by Sumiyoshi et al. (2011) to perform simultaneous high resolution EEG recording inside a 7T MRI scanner. After the EEG mini-cap fixation, a silicon-based probe (NeuroNexus Technologies), which consists of a linear shank with an array of iridium-oxide microelectrodes (i.e. area 177 $\mu m^2$, intervals 50 $\mu m$), was perpendicularly inserted at different depths into the cerebral cortex through an available hole in the EEG mini-cap (i.e. probe area). Arbitrarily, we employed silicon-based probes with either sixteen (*short probe*, 5 rats) or thirty-two (*long probe*, 4 rats) microelectrodes. The impedance of the microelectrodes in the probe ranges within the interval of 0.7-0.9 $M\Omega$. The impedance for all EEG electrodes was less than 50 $k\Omega$ in all experiments (Fig. 1 B, bottom), as determined by the *BrainVision Recorder* software (Brain Products GmbH). For the EEG recordings, the reference and ground electrodes (SEE203, GE-Marquette Medical Systems) were placed on the right and left ear-lobes, respectively.

*Insert figure 1 around here*

In all experiments, the penetration length and insertion angle of silicon-based probes were accurately monitored/corroborated through a micromanipulator's control system (SM5, Luigs & Neumann) and the Bregma stereotaxic coordinates (Paxinos and Watson 2007).

**Electrophysiological recordings**

High-resolution intracranial electrical recordings were obtained using amplifiers at 25 *kHz* (PZ2, Tucker and Davis Technologies, Inc. "TDT") connected by an optical fiber to

a signal processing unit comprising eight parallel CPUs (RZ2, TDT) and by a coaxial cable to a preamplifier located inside an acute 16-channel 18-bit hybrid headstage. Extracellular potentials were collected online using a *logic/symbolic programming language* supported by the signal processing unit (OpenEx software, TDT). To obtain LFPs from the raw data, we applied a Butterworth band-pass filter with cutoff frequency set between 1 *Hz* to 500 *Hz*. Event-related LFPs, corresponding to whisker deflections, were calculated by averaging stimulus-locked LFP responses over a large number of trials (> 100). To detect unit activity, a band-pass filter with cutoff frequency set between 500 *Hz* to 8 *kHz* was also applied to the raw data. Then, we extracted neuronal spikes by negative edge detection with a threshold of 4 times the standard deviation and 1.5 *ms* dead time. Twenty samples (i.e. eight samples prior and twelve samples posterior to the minima) of the detected spikes were used for classification. The spikes at each microelectrode were classified into putative PCs and SS cells (Ogawa et al. 2011; Goto et al. 2012). The spike time events were used as the triggers to compute spike-related potentials (SRPs) for each particular classified cell. EEG recordings (32-channels) were obtained using commercial EEG amplifiers (BrainAmp MR, Brain Products GmbH), with 10 $M\Omega$ input impedance, 2 $\mu Vpp$ input noise, > 90 *dB* in-phase suppression and +/-16 *mV*/500 *nV* signal range/resolution. The EEG digitalized signal was band-pass filtered online using software-controlled digital filters, i.e. the lower and upper cut-off was set at 0.016 *Hz* and 1000 *Hz*, respectively. An equivalent large number of single trials were used to estimate the event-related EEG signals from stimulus-locked EEG responses.

**Whisker stimulation protocol**

We used both a single and a whole whisker deflection protocol to stimulate the left vibrissae system of the rats. In both cases, the whiskers were shortened to 1 *cm* in length and deflections were carried out from rostral to caudal direction. Single whiskers were deflected by a piezoelectric bimorph actuator (TAYCA, Japan) that was controlled by a piezo-driver (PCD-001, General Photonics, USA). The deflection angle, frequency and interval for each stimulus were set to 7.2 *degree*, 1 *Hz* and 100 *ms*, respectively. Whole whiskers were deflected by short (10 *ms* in duration) air-puffs delivered from the rostral to the caudal direction. The needle's tip used for stimulation was placed around 2 *cm* away from the rat's jaw and approximately parallel to its snout. The air-puffs were

generated from a high-pressure air tank controlled by a pneumatic pico-pump (PV830, World Precision Instruments) at a pressure of 15 *psi*. The frequencies of air-puff stimulation were 1 *Hz* and 3 *Hz*. A program in MATLAB (Version 7.5.0.342, R2007b, The MathWork Inc.) was used to automatically control the operating devices (i.e. RZ2, BrainAmp MR, PCD-001 and PV830) through a multiple input/output AD converter (PCI-6259, National instruments, USA), as well as to generate the desired triggers for the stimulation and recording (i.e. to perform off-line analyses) devices.

**MRI anatomical imaging**

High resolution T1-weighted anatomical images were acquired on a 7T MRI scanner with a maximum gradient of 300 *mT/m* (70/16 Pharmascan, Bruker Biospin, Germany) using a 38 *mm* rat brain quadrature resonator for RF transmission and reception. The rats were placed onto a head holder comprised of a tooth bar. Under inhaled isoflurane anesthesia (5 % induction and 2 % maintenance), the animals were kept warm with water circulating at 37 *°C*. Volumetric images were acquired using a T1-weighted 3D RARE sequence with fat suppression, 300/8.5 *ms* TR/TE, RARE factor 4, 100 *kHz* spectral bandwidth, 8 averages, 3.4×3.4×3.84 $cm^3$ FOV, 256×256×128 image matrix, and 125×125×300 $\mu m^3$ voxel resolution. The T1-weighted anatomical images (*supplementary video 1*) were obtained two days previous to the electrophysiological experiment, with a total acquisition time of four hours and five minutes. During MRI experiments, the rats were anaesthetized with isoflurane (0.5-1.5 %) mixed in pure oxygen.

**Immunostaining**

Coronal sections (100 $\mu m$ in thickness) of the entire barrel cortex were obtained from the postmortem fixed brains of those rats used for the concurrent EEG and LFP experiments. In contract, the rat brains were sectioned tangentially to the cortical surface for the volumetric LFP experiment. In order to reveal the barrels, sections were treated with 3,3'-diaminobenzidine (DAB, Sigma) and cytochrome C oxidase from horse heart (Sigma) (Riera et al. 2010a). Fluorescent Nissl staining of the brain sections was additionally performed to determine the relative position of the silicon-based probe with respect to the cortical layers. Immunostaining images were obtained by using an upright fluorescent microscope (SZX16, Olympus). In order to co-localize the silicon-based probe and the layers/barrels, shanks were submerged before insertion in a solution containing lipophilic

neuronal tracer carbocyanine (DiI, Invitrogen).

**CSD analysis**

To analyze the distributions of diminutive electric sources $s = -\sigma\nabla^2\varphi$ [*] inside a mesoscopic region (i.e. a cortical barrel), we used the volumetric (vCSD, Goto et al. 2012, a MATLAB code developed in our laboratory) and the inverse (iCSD, Pettersen et al. 2006; **iCSDplotter** software, version 0.1.1[+]) CSD methods.

The parameters used in the vCSD method were: **a)** the inter-grid distance $\Delta$, which was 50 $\mu m$, and **b)** the radial/tangential conductivities and radii for all cortical layers, which were previously estimated by Goto et al. (2010) for the somatosensory cortex of adult Wistar rats. We applied the average reference operator (Pascual-Marqui 1999) to the Green's function matrices, event-related LFPs and SRPs in order to remove undesirable signals from the reference electrode (Bertrand et al. 1985). The parameters used in the iCSD method were: **a)** the disk diameter $d$ for the sources (i.e. the barrels), which was 0.5 *mm*, **b)** the standard deviation for the Gaussian filter, which was 50 $\mu m$, the thickness of the cortical columns for the barrel cortex $l$, which was 2 *mm,* and **c)** the mean electric conductivity σ (homogenous media) for brain tissues, which was 3 *mS/cm*.

For both methods, we did not use boundary conditions (i.e. free electric potentials). In order to estimate the laminar/volumetric current sources associated with particular neuronal activities, we applied the iCSD/vCSD method to the event-related LFPs and SRPs obtained in each experiment. The mathematical definition of multipolar moments [e.g. monopoles $m(t)$, dipoles $\mathbf{d}(t)$ and quadrupoles $\mathbf{Q}(t)$] from the volume sources $s$ in a volume of interest $V$ are given by equations:

$$m(t) = \int_V s(\vec{r},t)\, d\vec{r}^3$$

$$\mathbf{d}(t) = \int_V s(\vec{r},t)(\vec{r}-\vec{r}_m)\, d\vec{r}^3 \qquad (1a)$$

$$\mathbf{Q}(t) = \int_V s(\vec{r},t)(\vec{r}-\vec{r}_m)(\vec{r}-\vec{r}_m)\, d\vec{r}^3$$

In particular, for the iCSD method, these equations take a simplified form:

[*]The magnitude $s$ is named volume source and has dimensions of μA/mm$^3$.

[+]**iCSDplotter** download: http://bebiservice.umb.no/projects-public/cnsweb/wiki/Miscellaneous/Downloads

$$m_z(t) = \pi\left(\frac{d}{2}\right)^2 \int_0^l s(z,t)\,dz$$

$$d_z(t) = \pi\left(\frac{d}{2}\right)^2 \int_0^l s(z,t)(z - z_m)\,dz \qquad (1b)$$

$$Q_z(t) = \pi\left(\frac{d}{2}\right)^2 \int_0^l s(z,t)(z - z_m)^2\,dz$$

Assuming the barrel columns are perfect cylinders, their volumes $V = \pi(d/2)^2 l$ would be 0.39 $mm^3$. The vector $\vec{r}_m$ indicates the center of gravity of the cortical column, and the value $z_m$ stands for its respective laminar coordinate. The axis z is defined in the direction perpendicular to the neocortex with positive and negative values toward the supragranular and infragranular layers, respectively. The integrals above were evaluated numerically using a trapezoidal method, where each subinterval corresponds to a particular grid point in the corresponding CSD method.

**EEG forward/inverse problem**

In order to relate the observed electric potentials and their causing current source configuration inside the brain, the rat's head was modeled as an isotropic and piece-wise homogeneous volume conductor. There was no skin tissue in the area where the electrodes were located; hence, the brain and the skull constituted the main tissue compartments. The positions of the electrodes were defined from pictures taken during the experiments and landmarks on the 3D-reconstructed T1-weighted anatomical references (*supplementary video 2*). The skin tissue was ignored since it was removed above the interaural axial plane (red dashed-line). Realistic shapes for the surfaces limiting the abovementioned tissue compartments were segmented and triangulated (*supplementary video 2*). We employed 642 triangles per surface, i.e. 1280 vertexes. The conductivities used for brain and skull compartments were 2.9 $mS/cm$ (Nunez and Srinivansan 2006) and 0.13 $mS/cm$ (Oostendorp et al. 2000), respectively.

In general, an electric potential $v(\vec{r}_e,t)$ [*] at any position $\vec{r}_e$ on the skull produced by a continuous field of microscopic electrical sources $I(\vec{r},t)$ (dimensions : $I \sim \mu A/mm^3$ )

[*]Physical dimensions: $\mu V$

inside the brain $R$ can be represented by an inhomogeneous Fredholm integral equation of the second kind (2), with the secondary currents $\mathbf{j}_k(I,\vec{r}) = (\sigma_{k+1} - \sigma_k) v_k(I,\vec{r}) \mathbf{n}_k(\vec{r}) / \Delta l$ defined for each elemental volumetric shell $\Omega_k$ (i.e. the surface $S_k$ of thickness $\Delta l \to 0$). The symbol $\sigma_k$ denotes the conductivity of the *k*-th compartment (i.e. brain, skull), and $\mathbf{n}_k(\vec{r})$ is the normal vector to the surface $S_k$ at location $\vec{r}$. The current source can be interpreted in terms of the electrical charge density as $\rho(\vec{r},t) \to I(\vec{r},t)/\sigma$. The theoretical foundations and numerical strategies for calculating surface potentials $v_k(I,\vec{r})$ are given in Hämäläinen and Sarvas (1989).

$$4\pi\sigma v(\vec{r}_e,t) = 4\pi\sigma v_0(\vec{r}_e,t) + \sum_k \int_{\Omega_k} \mathbf{j}_k(I,\vec{r}) \cdot \nabla \left( \frac{1}{|\vec{s} - \vec{r}|} \right) d\vec{r}^3 \qquad (2a)$$

$$v_0(\vec{r}_e,t) = \frac{1}{4\pi\sigma} \int_R \frac{I(\vec{r},t)}{|\vec{r}_e - \vec{r}|} d\vec{r}^3 \qquad (2b)$$

Let us assume $I(\vec{r},t) = \begin{cases} s(\vec{r},t) & \vec{r} \in V \\ 0 & \vec{r} \notin V \end{cases}$, where $V$ is a specific mesoscopic volume centered at $\vec{r}_m$. If the observation site $\vec{r}_e$ is far enough from the center $\vec{r}_m$, then $v_0(\vec{r}_e,t)$ can be written as a function of the multipolar moments:

$$v_0(\vec{r}_e,t) = \frac{1}{4\pi\sigma} \left[ \frac{m(t)}{|\vec{r}_e - \vec{r}_m|} + \mathbf{d}(t) \cdot \nabla_{\vec{r}_m} \left( \frac{1}{|\vec{r}_e - \vec{r}_m|} \right) + \frac{1}{2} \mathbf{Q}(t) : \nabla\nabla_{\vec{r}_m} \left( \frac{1}{|\vec{r}_e - \vec{r}_m|} \right) + \cdots \right] \qquad (3)$$

The scalar product $\mathbf{a} \cdot \mathbf{b}$ and the tensor contraction $\mathbf{A} : \mathbf{B}$ are defined in Jerbi et al. (2002). Generalizing this concept to include contributions from all cortical columns, with the proper substitution of multipolar moments by their respective densities in a macroscopically continuous sense, and also from other mesoscopic regions of the brain, we obtain:

$$v_0(\vec{r}_e,t) = \frac{1}{4\pi\sigma} \left[ \int_R \frac{m(\vec{r},t)}{|\vec{r}_e - \vec{r}|} d\vec{r}^3 + \int_R \mathbf{d}(\vec{r},t) \cdot \nabla_{\vec{r}} \left( \frac{1}{|\vec{r}_e - \vec{r}|} \right) d\vec{r}^3 + \right. \\ \left. + \int_R \frac{1}{2} \mathbf{Q}(\vec{r},t) : \nabla\nabla_{\vec{r}} \left( \frac{1}{|\vec{r}_e - \vec{r}|} \right) d\vec{r}^3 + \cdots \right] \qquad (4)$$

Under the assumption of the dipolar model, the final EEG forward problem is represented by equations (2a) and (5).

$$v_0(\vec{r}_e,t)=\frac{1}{4\pi\sigma}\int_R \mathbf{d}(\vec{r},t)\cdot\nabla_{\vec{r}}\left(\frac{1}{|\vec{r}_e-\vec{r}|}\right)d\vec{r}^3 \quad (5)$$

EEG recordings $v^e_{t_k}=v(\vec{r}_e,t_k)-v(\vec{r}_r,t_k)$ constitute discrete observations in time $t_k$ ( $k=0,\cdots,N_T$ ) and space $\vec{r}_e$ ( $e=1,\cdots,N_e$ ), which are always contaminated with observational noise $e^e_{t_k}$ and measured with respect to a common reference electrode $\vec{r}_r$. For biophysical reasons (Baillet et al. 2001), it is feasible to assume that most of the EEG signal comes from the cortical surface. Therefore, it is worthwhile to set $\mathbf{d}(\vec{r},t)$ different from zero only on the cortical surface. The dipolar moment has been assumed to originate from postsynaptic currents caused mainly by the activation of PCs perpendicular to the cortical surface (Hämäläinen et al. 1993; Okada et al. 1997). Therefore, the vector current source can be written as $\mathbf{d}(\vec{r},t)=\boldsymbol{\mu}(\vec{r})d(\vec{r},t)$, with $\boldsymbol{\mu}(\vec{r})$ and $d(\vec{r},t)$ representing the normal direction to $\Gamma$ (from the white matter to the external brain surface) and the time varying dipole amplitude, respectively. The EEG forward problems can be finally written as generalized linear convolutions (6), with kernel $h(\vec{r}_e,\vec{r})$.

$$v^e_{t_k}=\int_\Gamma h(\vec{r}_e,\vec{r})\,d(\vec{r},t_k)\,d\vec{r}^2+e^e_{t_k} \quad (6)$$

The kernel for the EEG forward problems can be defined from equations (3-5) in Hämäläinen and Sarvas (1989), with particular considerations for the electric potential in the infinite homogeneous medium (5). This represents a scalar boundary element method incorporating deflections and an isolated problem approach. This boundary element method was implemented in MATLAB*. The numerical evaluation of the kernel in equation (6), for a particular electrode, on the triangulated cortical surface of an individual rat is shown in the *supplementary video 2*. In this paper, the EEG forward problem is used to perform the equivalent dipole fitting by a least square strategy (Jones et al. 2007) and the surface LORETA inverse solution (Riera et al. 2000).

# III. Results

Since the vibrissae system in rodents is very well-documented (Petersen 2007), electrophysiological data recorded from rats under a whiskers stimulation paradigm will

*The code is available on request by email: riera@idac.tohoku.ac.jp

be of great utility to understand the nature of the neocortical current sources on the mesoscopic scale, as well as to quantify the relationships they keep with the macroscopic data.

## *vCSD analysis*

In a first experiment, we applied the vCSD method to estimate from three-dimensional recordings of extracellular potentials the intra-cortical multipolar moments generated either by spiking neurons (i.e. PC, SS) or during their synchronized population postsynaptic activity. PCs have been considered the primary sources of the LFP, as well as of the EEG, while SS cells are assumed to produce no resultant extracellular electric potentials due to their closed-field configuration. As a result of technological limitations in the past, a precise validation of these properties through a quantification of the actual electric currents generated by these two major cortical neurons is lacking. Here, we made use of a method for vCSD analysis (Goto et al. 2012) to evaluate the main characteristics of the current sources generated by single cortical neurons in two different situations: a) spiking and b) experiencing synchronized postsynaptic potentials.

Figure 2 A (top-left) shows the grand-average of SRPs obtained for 10 putative layer IV PCs. The corresponding time courses of the monopolar, dipolar and quadrupolar components estimated from these SRPs, and associated with back-propagating spikes along the PCs, are shown in the panels on the bottom-left. Note that at the time of maximum dipolar component (i.e. brown-dashed-vertical line), this type of cell shows a bipolar current source configuration (Fig. 2 A, top-right), as expected with a preferential orientation perpendicular to the cortical surface (Fig. 2 A, bottom-right). To our knowledge, this study provides the first quantitative evaluation of the maximal dipolar current generated by spiking PCs (*z-direction*, 49.7±22.0 *nA mm*; t-test significant, $p < 0.01$). Surprisingly, we found also a monopolar (–11.7±3.4 *nA*, Fig. 2 C) component that was significant at the negative-peak of the spike (black arrow). Even though non-balanced redistributions of the electric charge exist at each time instant, the net charge at a large temporal scale (i.e. 4 *ms*) was zero (Fig. 2 A, green dashed-line). Finally, the quadrupolar component produced by back-propagating spikes in this type of neuron was also significant (51.2±39.1 $nA\ mm^2$; t-test significant, $p < 0.05$). Therefore, here we

confirmed experimentally a previous theoretical result by Milstein and Koch (2008) about the need of including dipolar and quadrupolar components when modeling the mesoscopic scale ($r < 1$ *cm*), with the difference that additionally we provided evidence for a substantial role of the monopolar term. The grand-average of SRPs obtained for 10 putative SS cells as well as the respective statistics for the multipolar components are shown in figure 2 B (top-left). As assumed in many previous studies, SS cells have a very symmetric current source configuration (Fig. 2 B, top-right) resulting in neither significant dipolar nor quadrupolar components (Fig. 2 B, bottom-right) at the time instant of maximal activation (brown-dashed-vertical line). Although it was apparently different from zero, the monopolar component at the peak of the spike (black arrow) was not statistically significant (i.e. $-6.7 \pm 0.7$ *nA*, Fig. 2 C) and, as for the PCs, the net charge at the large temporal scale was also zero (Fig. 2 B, green dashed-line).

*Insert figure 2 around here*

Event-related LFPs reflect concurrent electric activity in the dendrites of large PCs over an extended cortical area. Hence, we used them to evaluate whether or not multipolar components, similar to those previously observed for back-propagating spikes along PCs dendrites, appear also when many of these PCs receive synchronized synaptic inputs. First, we estimated the volume current sources $s$ for both single and whole whisker stimulation paradigms by applying vCSD to the corresponding event-related LFPs. Thanks to the DiI histological images, we were able to co-register for each single condition the image of the estimated $s$ and that of the anatomical barrels (Fig. 3, top-right). From visual inspection, we confirmed that the probe covered always about nine barrels. To determine the multipolar moments generated by each independent barrel, we used a single whisker stimulation protocol. For each deflected whisker, we applied a spike sorting method to identify the most active barrel and determined its anatomical border from tangential sections of the brain with the cytochrome C oxidase immunostaining. The anatomical barrel of the corresponding deflected whisker was used as the volume of interest $V$ in equation (1a) to calculate the multipolar moments associated with the barrel-wise postsynaptic evoked activity. A grand-average CSD spatiotemporal map was obtained from pooling the volume sources $s$ along the x-y directions within each particular activated barrel and then summing the resulting maps for

all rats (Fig. 3, top-left) shows. Barrels that were in the border of the region covered by the three-dimensional probe were not included in the statistical analysis. The mean and standard deviation of the multipolar moments obtained from single deflected whiskers for all rats are shown on figure 3 (bottom-right). As expected, a dipolar component at the maximal postsynaptic activity (–0.43±0.16 $\mu A\ mm$; t-test significant, $p < 0.01$) was predominantly tangential to the cortical surface. Significant monopolar (–0.44±0.20 $\mu A$; t-test significant, $p < 0.01$) and quadrupolar (0.13±0.06 $\mu A\ mm^2$; t-test significant, $p < 0.01$) components associated with synchronized postsynaptic activity within single barrels were also observed at the time of maximal evoked response. We applied a whole whisker stimulation protocol to evaluate whether or not temporal unbalances in the charge redistributions would remain observable for volumes covering a larger cortical surface. For that end, we used the whole cortical region defined by our three-dimensional probe (i.e. 2.5 $m^3$-voxel) as the volume of interest in eq. (1), which represents the most elemental volume in modern EEG imaging methods. For each rat, we were able to observe about four functional barrels (*supplementary video 3*). At the time instant of maximal evoked neuronal activity, we found significant monopolar components within the mesoscopic voxels (–3.32±1.20 $\mu A$; t-test significant, $p < 0.05$) (Fig. 4). In both cases above, the net charge at a large temporal scale (i.e. 200 *ms*) was approximately zero (Figs. 3 and 4, green dashed-lines).

*Insert figures 3 and 4 around here*

## Concurrent LFP and EEG recordings

In a second experiment, we used concurrent recordings of high-resolution skull EEG and laminar local field potentials to evaluate the relationship between intra-cortical multipolar moments and the EEG equivalent dipoles for the Wistar rat's head. To improve the signal-to-noise ratio for the EEG recordings, we used a whole whisker stimulation protocol in this experiment. Intracranial electrical recordings were obtained at different depths from the pial surface using both short and long probes, covering the entire cortical lamina with data from different rats. In order to co-register data from all experiments, we utilized cytochrome C oxidase, Nissl bodies and DiI neurotracer staining images from the postmortem fixed brain sections (Fig. 5 A, left). The relative position of the shank with

respect to the barrels (grey areas enclosed by cyan boxes) and septums (inter-spaces indicated with arrows) was estimated from the cytochrome C oxidase immunostaining, as was clearly defined at the level of layer IV, and the DiI fluorescent images. For all experiments, the probe (red trace, DiI) was roughly perpendicular to the cerebral cortex, and remained within a single column (i.e. a barrel) along all cortical layers. Hence, we assumed that the recorded LFP for the most part reflected neuronal activity mainly from a single barrel. Layers distributions were determined through the Nissl staining as was indicated in the combined image (Fig. 5 A, right). The interfaces between layers V-VI were easily determined from jumps in the distributions of the large PCs. The limits of layer IV were evident from the intensity of the immunoreactions to cytochrome C oxidase. Layer I was characterized by a low density of Nissl bodies. In each recording, the microelectrodes in the probe covered a region of about either 800 $\mu m$ or 1600 $\mu m$ in length for the short and long probes, respectively. A typical example of the event-related LFP recorded with a short probe is shown in figure 5 B (top). In this case, the spatiotemporal pattern is consistent with LFP observations from a region between layers II/III (middle) and V. Figure 5 B (bottom) shows the corresponding CSD analysis for this particular LFP data. By imposing a boundary condition on the volume sources at the pial surface $s(z)\big|_{z=l} = 0$ and at the interface with the grey matter, the iCSD method is able to estimate the current sources from deeper layers up to the most superficial layers. A small standard deviation was observed from the inter-rat CSD statistics analysis, which indicates a reproducibility of the CSD maps for the entire barrel cortex (data not shown).

*Insert figures 5 around here*

After co-registration, we were able to create, from all trials and rats, a grand average color map of the event-related CSD of the entire barrel cortex (Fig. 6, top color panels). At each time instant, we estimated the center of charge $z_c$ as that cortical depth for which positive and negative net charges were equally distributed on both sides.

$$z_c(t) = \min_{z_m} \int_0^l s(z,t)\left|z_m - z\right| dz \qquad (7)$$

We found that the center of the charge in the neocortex fluctuated very rapidly with time, although it seemed quite stable shortly after the stimulus onset. The spatiotemporal

patterns were very similar to those reported in a previous work (Di et al. 1990; Fig. 3, personal communication with Barth D). In our experiment, 1 *Hz* stimulus frequency constitutes the closest condition to that used in this previous study. For that particular condition, the main common characteristics between our CSD pattern and that found by Di et al. (1990) were: *a*) an early sink in layers II/III-IV with a very short duration, *b*) at the level of layer IV, this sink was followed by a long-lasting weak source, *c*) the peak amplitude of such a source component delayed and intensified while approaching layer V, *d*) there was a rapid change of polarity in layer V soon after the stimulus onset, *e*) a short source at layer VI was followed by a non-pronounced but longer sink. In our case, there was also an early source in layer I, but it was not followed by an extended sink as in that previous work. Similar spatiotemporal patterns for the earliest time window (up to 50 *ms* after the stimulus onset) have been reproduced in more recent studies (Higley and Contreras 2007; Mégevand et al. 2008). Note that in these last two studies, the colors yellow/red and blue are used for sinks and sources, respectively. We also observed symmetrical source arrangements (i.e. sink/source/sink patterns) around layer IV, which are distinguished in Mégevand et al. (2008, Fig. 2). Such a CSD profile may be associated with the early activation of spiny stellate cells, the main target of thalamocortical axon terminals. The time courses of the current sources presented in this paper seem to be shifted fifteen milliseconds with respect to those observed in previous studies. We employed a two meters silicon tube from the high-pressure air tank to the needle's tip, which introduced an undesirable delay in the deflections of the whiskers. In the abovementioned previous studies, electromechanical devices (i.e. piezoelectric stimulators) were used. Furthermore, in our experimental paradigm, all left whiskers were simultaneously deflected, while in two of these previous studies selective whiskers were stimulated (Di et al. 1990; Higley and Contreras 2007).

We calculated the multipolar moments by using equations (1b). The time courses of the multipolar moments with respect to the center of gravity of the cortical column are shown in figure 6 (bottom panels, red continuous-line). Also shown are the time courses when the center of charge was used instead (black dashed-lines), which produced dipolar and quadrupolar moments with questionable waveforms. In agreement with our first findings, there were robust contributions from the monopolar and quadrupolar components to the

mesoscopic volume sources in the barrel cortex. The maxima amplitude of the monopolar and dipolar currents, generated by a single barrel, was approximately the same, while it was relatively smaller for the quadrupolar current. Despite of the similarities in the time courses of the multipolar moments in figures 3 and 6, they differ in numerous features. Differences in the stimulation protocols (i.e. single vs. whole whisker), the probe formats (i.e. laminar vs. three-dimensional) and the source model (i.e. cylindrical symmetry and smoothing) might underlie such discrepancies.

*Insert figure 6 around here*

The event-related EEG signals at all electrodes for 1 *Hz* and 3 *Hz* are shown in figure 7 (A, top), which revealed the presence of four main components along the time course (C1-C4, marked with vertical blue lines). The topographic color map* of each component is shown in the respective bottom panels for both stimulus frequencies. The expected contra-lateral components were not only in the primary and secondary somatosensory cortices but also in a large portion of the motor cortex, as can clearly be identified from these topographic maps (Petersen 2007; Mégevand et al. 2008; Boorman et al. 2010). Ipsi-lateral activation of the primary somatosensory cortex is also exposed. The spatiotemporal event-related EEG topographic maps for a particular rat are shown in *supplementary videos 4* (conditions: A – 1 *Hz*, B – 3 *Hz*). Similar topographic patterns in space and time were found in all rats. In order to quantify the reproducibility among rats, we estimated not only the event-related EEG signals but also the standard deviations for all electrodes and stimulus frequencies. As shown in figure 7 (B) for electrode #14, the signal-to-noise ratio was adequate and the EEG data was very reproducible.

*Insert figure 7 around here*

In this study, we estimated two particular types of EEG inverse solutions (i.e. least square dipolar fitting and surface LORETA, table I) from the skull EEG data. First, we estimated the time varying amplitude of an equivalent current dipole by a least square fitting strategy (Jones et al. 2007). This equivalent current dipole was placed in the center of the barrel field for each rat, which was determined by semi-automatically co-registering the T1-weighted anatomical images with a digitalized atlas of the Wistar rats (Paxinos and

*The topographic maps are plotted on the rat's actual skull

Watson 2007). The direction of this equivalent current dipole was set perpendicular to the cortical surface and positioned at a depth of 1 *mm*. Following the methodology suggested by Jones et al. (2007), we estimated the additional free moving equivalent current dipoles until the goodness-of-fit was larger than 75 %. We used the $\chi^2$ criterion for the goodness-of-fit assuming that the EEG data p.d.f. was Gaussian. The effect of these free moving dipoles was removed from the data using the signal-space projection method. The final waveform of the equivalent current dipole in the barrel field was refitted to the residual (Fig. 8, upper panels). Second, the surface LORETA was implemented using the discrete Laplace-Beltrami operator for the cortical surface as the regularizing matrix (Riera et al. 2000). To avoid singularities in the regularizing matrix due to the harmonic subspace (i.e. the constant functions), we disconnected the vertexes of the left and right hemispheres, which was equivalent to introducing a boundary condition at the level of the corpus callosum. The topographic maps on the cortex obtained from the surface LORETA were not in disagreement (*data not shown*) with previous findings obtained using other neuroimaging techniques (voltage sensitive dyes – Ferezou et al. 2007; fMRI – de Celis Alonso et al. 2008). We pooled the amplitudes of the surface LORETA inverse solution for vertexes in close proximity to the center of the barrel field, which allow us to have a time series for each rat equivalent to that obtained from the least-square dipolar fitting (Fig. 8, lower panels).

*Insert table I around here*

*Insert figure 8 around here*

The final result of the source analysis is a waveform $d_{IS}^{F}(t)$ for each inverse solution type "*IS*" and stimulus frequency "*F*". In order to evaluate the impact of multipolar components on large-scale observations, we performed a linear regression analysis (8) for each rat. In this analysis, which was motivated by the particular dependency of the multipolar moments (i.e. $m_z$, $d_z$ and $Q_z$) in the equation (4), the time courses of the normalized multipolar moments obtained from the small-scale LFP data through equations (1) (Fig. 6, bottom panels) were used as known linear regressors (*"loadings"*) of the waveforms $d_{IS}^{F}(t)$.

630 $$d_{IS}^{F}(t)=\chi_{c}^{\{IS,F\}}+\chi_{m}^{\{IS,F\}}m_{z}(t)+\chi_{d}^{\{IS,F\}}d_{z}(t)+\chi_{Q}^{\{IS,F\}}Q_{z}(t) \quad (8)$$

631 The coefficient $\chi_{c}^{\{IS,F\}}$ was introduced to account for any difference in the baseline.
632 Figure 9 illustrates the result of such a linear regression from a particular rat for both
633 dipole-fitting (upper panels) and LORETA type of inverse solution (lower panels). The
634 respective estimated coefficients $\chi_{L}^{\{IS,F\}}$, $L=\{c,m,d,Q\}$, obtained from all rats, for both
635 type of inverse solutions and stimulation frequencies are shown in figure 10. In order to
636 compare the contributions from these multipolar moments to the large-scale waveforms
637 $d_{IS}^{F}(t)$, we performed a two-way ANOVA with multiple comparisons. The current
638 monopoles were the most significant source component of the $d_{IS}^{F}(t)$ waveforms. The
639 current monopoles were relatively larger for the 3 *Hz* stimulation condition, while
640 quadrupolar contributions were larger for the 1 *Hz* stimulation condition. The equivalent
641 current monopolar and quadrupolar components have opposite signs for both stimulation
642 conditions. These characteristics were very well-captured by both types of inverse
643 solutions. The dipolar components were positive for the 1 *Hz* stimulation condition, but
644 revealed a change in polarity between dipole-fitting and LORETA inverse solution for
645 the 3 *Hz* stimulation condition. The estimated macroscopic dipoles in the barrel cortex
646 revealed a dynamic content that resemble mesoscopic monopolar components more
647 prominent for the surface LORETA inverse solution than for the dipole-fitting one. The
648 goodness-of-fit for each inverse solution are summarized in table II. As expected, the
649 surface LORETA inverse solution provided always the best goodness-of-fit. Finally, we
650 evaluated the contribution of each multipolar regressor to the large-scale waveforms
651 $d_{IS}^{F}(t)$ by combining the same linear regression analysis with a "*leave one out*" strategy.
652 In the leave one out strategy, we performed a linear regression analysis with only two
653 multipolar regressors, leaving one of them (e.g. monopole, dipole, quadrupole) out of the
654 linear model (8). The estimation errors (table II) clearly revealed a major contribution to
655 $d_{IS}^{F}(t)$ of the monopolar current sources.

656 *Insert figures 9 and 10 around here*

657 *Insert table II around here*

# IV- Discussion

Based on recent advances in both techniques for electrophysiological recording and methodologies for CSD analysis, we have revised in this study significant biophysical aspects of the genesis of extracellular potentials. Keeping in agreement with previous experimental data, we observed that cortical PCs are the cells that contribute the most to both the small-scale LFP and large-scale EEG data. However, for the first time quantitative values of the actual electric currents produced by PCs, either while spiking or during the integration of synchronized postsynaptic potentials, are provided. As suggested theoretically in the past (Milstein and Koch 2008), we found that not only dipolar but also quadrupolar components emerge in the LFP up to distances of almost 1 *cm*. More important, we presented evidence for a remarkable unbalance in the instantaneous charge redistribution during different types of neuronal activation, at least for the sampling rate normally used to observe electrophysiological signals. Based on a linear regression analysis, we examined the similarities between the dynamics of each multipolar component reconstructed using intracranial laminar LFP from the barrel cortex and the one of an equivalent dipole estimated from the skull-EEG data. Unexpectedly, the time series of the equivalent EEG dipole were much better represented by the intra-cortical monopolar loadings than by the dipolar ones. Signs of the intra-cortical quadrupolar components were found in the skull EEG, but by some undetermined reasons, the regression coefficients were consistently negative. In the particular case of Wistar rats, the electrodes are positioned very close to the cortical current sources (~ 1 *cm*), a fact that may lie beneath the existence of quadrupolar components for EEG data in this study. These last results indicate that any EEG inverse solution based on a dipolar model will comprise not only the mesoscopic dipolar components but also those monopolar and quadrupolar ones. Our conclusions are founded on data recorded from the barrel cortex of Wistar rats, a cortical region that has been very well studied in the past. Regardless several particulars for the barrel field, columns in other cortical regions of mammals share many similarities with the barrels in terms of the laminar organization, cellular distribution/orientation and microscopic circuitries. Therefore, we conjectured here that our results about the multipolar profile of the LFP are valid for the neocortex in general. However, our conclusions about the contributions of the intra-cortical multipolar

moments to the EEG macroscopic observations will definitely depend on the size of the head for each particular species as well as on the relative position of the EEG electrodes respect to the cortical mesoscopic patch of interest.

**Plausible scenarios for a mesoscopic CSD unbalance**

The existence of unbalanced current sources in the neocortex constitutes one of the most provocative findings of this study. The introduction of monopole current source models to describe EEG data might raise questions about whether or not any well-established laws of physics are violated. Here, we propose two scenarios to rationalize this result without having to assume that electrical charge is either created or destroyed. First, note that, at any location, the temporal average of the monopole current source was zero, consequently no charge accumulates anywhere over time. Then, the CSD unbalance is an issue related to the relative timescales for both the charge movements and the observed EEG signals. To solve the EEG forward problem, we generally assume that the total electric current $\vec{\mathbf{J}}_{Total}(\vec{r},t)$ inside any mesoscopic area in the brain is defined as a superposition of non-dispersive ohmic electric currents $\vec{\mathbf{J}}_{Ohm}(\vec{r},t)=\vec{\vec{\sigma}}(\vec{r})\vec{\mathbf{E}}(\vec{r},t)$ and of certain "*impressed*" current sources $\vec{\mathbf{J}}_{P}(\vec{r},t)$. The magnitude $\vec{\mathbf{E}}(\vec{r},t)$ represents the electric field and $\vec{\vec{\sigma}}(\vec{r})$ is the conductivity tensor of the brain tissues. Hence, it is believed that any charge movement in the brain tissue is only caused by the action of an electric field. Under the validity of the quasi-static approach for the electromagnetic field, the EEG forward problem is then formulated as the solution of the principle of current conservation $\nabla\cdot\vec{\mathbf{J}}_{Total}(\vec{r},t)=0$.

*The first scenario: The spatial dependency of the tissues polarization*

It has been shown that, as a consequence of two major dielectric relaxation mechanisms (i.e. the counterion and interfacial polarizations), the brain tissues are highly dispersive for the frequency range of the electrophysiological recordings (Gabriel et al. 1996, 2009). Additionally, the conductivity and permittivity depend on the location (i.e. inhomogeneity) and direction (i.e. anisotropy) inside the brain (Gabriel et al. 2009; Goto et al. 2010). Therefore, as charge moves its effect on externally-measured fields can depend on location. Also, at the spatial scale of single cells, the charge moving in the

718 cytoplasm caused by a neuronal event will be detected with longer delays than that
719 moving along the interstitial space. Thus, in the timescale of EEG observations, it is
720 perfectly reasonable that for a current sink to appear temporarily as charge enters the cell,
721 to be replaced by a current source at a slightly later time as the charge leaves the cell. At
722 the level of a mesoscopic volume (e.g. a barrel), brain tissues may additionally behave
723 like a multiple spatial filtering device with frequency characteristics depending on
724 location/orientation. Bearing in mind that the LFPs are obtained through filters that
725 attenuates signals with frequencies higher than a cutoff-frequency (i.e. ~ 500 *Hz*), one
726 must be careful while assuming that any local closed-loop inside the tissue can be ideally
727 modeled as an RC circuit. Indeed, even though the total electric current is conserved
728 within a loop comprising two regions with different electric permittivity/conductivity
729 profiles, the *observed* electric currents (i.e. limited to a particular frequency range) may
730 look unbalanced to all appearances (*Appendix I-A*).

731 *The second scenario: Charge diffusion and buffering*

732 Chemical gradients and active transport mechanisms across cellular membranes cause
733 also significant charge movements in the brain tissues. For example, a significant
734 contribution of ionic diffusion currents perpendicular to the neuronal membranes inside
735 the neocortex have been recently estimated by Bédard and Destexhe (2009), which was
736 about hundred times greater than the ohmic electric current at 100 *Hz*. Consequently,
737 these authors represented any type of current source of the EEG as a superposition of a
738 finite number of monopolar sources. Alternatively, brain cells are endowed with a variety
739 of mechanisms to transport ions across their membranes. An example of that is the ion
740 pumping by the $Na^+/K^+$ and $Ca^{2+}$ ATPases in neurons to reestablish ion gradients after
741 the opening of voltage/chemical-dependent channels. Another example is the glutamate
742 recycling via the EAAT1&2 enzyme (Riera et al. 2008), which might implicate
743 considerable buffering of ions in the neocortex during an increase of the neuronal activity.
744 These principal buffering systems may also contribute to a redistribution of the electric
745 charge across the cellular membranes regardless of the principle of current conservation.
746 However, these mechanisms operate with a very low dynamic range and the CSD
747 unbalance reported in this study were in the order of few hundred of milliseconds. Hence,

buffering effects may cause CSD unbalances, but should not be considered as the major mechanism. A more detailed discussion about ion diffusion can be found in appendix I-B.

Finally, we would like to discuss possible undesirable situations that could bring about an apparent unbalance in the observed current sources. First, there exist many vessels and axons in the neocortex that could cause a shunting of electric currents to remote locations; and hence, bring about an apparent unbalance in the observed current sources. For example, electric current shunting by pial blood vessels has been reported in the past up to a 10% (Ranck 1963). Also, it has been proven that voltage fluctuations associated with dendro-somatic synaptic activity are able to propagate long distances along the axons (Shu et al. 2006), which may involve electrotonic current leakages from somas to faraway presynaptic terminals. In this study, the reference and ground for the intracranial electric recordings were on the skull and in close proximity to the barrel cortex. Consequently, we believe any electric current shunting through the vessels was minimized by this recording protocol. In order to evaluate the impact on the CSD distribution of any electric current shunting through the neuronal axons, in vivo simultaneous observations of intracranial and intracellular electric potentials are required in the future.

Second, based on previous results by Brankačk et al. (1993) readers may be concerned about alternations in the CSD profiles along the cortical layers for the particular case of using AC-coupled intracranial electric recordings. In particular, electrical potentials recorded with the PZ2 amplifiers (TDT) are AC-coupled through: **a)** a serial input capacitor (4.7 $\mu F$) connected in parallel with a grounded-resistance of 100 $k\Omega$ and **b)** a serial output capacitor (0.1 $\mu F$). Trivially, given that the CSD analysis results from applying a linear operator on the observed electric potentials at each time instant, a common AC-coupling to all electrodes will cause no alteration in the instantaneous CSD charge balance. Furthermore, we verified that event-related LFP associated with single whisker deflections showed typical waveforms for all shanks in the silicon-based probes. Hence, spatial distortions of the LFP caused by either an incomplete/unequal recovery or damage of the brain tissue were ignored. In the analysis, we did not include any experimental data containing suspicious artifacts, and we excluded those animals with bleeding and/or swelling around the cortical region of interest. Therefore, we hypothesize

779 that it is the limitations in the time resolution to observe extracellular potentials together
780 with either the spatial dependency of the dispersive relationships in the cortical tissues or
781 the ion buffering/diffusion effects what actually underlie the existence of the monopolar
782 components reported in this study.

783 **The equivalent current dipole in the neocortex**

784 In the past, when constructing theoretical frameworks to simulate the genesis of EEG and
785 MEG data, microscopic current sources had been assumed to be miniaturized intracellular
786 dipoles acting on the external medium. In particular, Yoshio C. Okada's group in
787 Albuquerque studied how the intrinsic ionic conductances (ligand- and voltage- sensitive)
788 and the morphology of PCs impact on the spatiotemporal characteristics of such
789 intracellular dipoles, and hence on macroscopic observations. In a pioneering work,
790 Murakami et al. (2002) proposed a single theoretical framework to interpret both small
791 (intra- and extra-) cellular potentials and MEG data recorded from hippocampal slices
792 (0.4 *mm* thick, about 6 *mm* wide and 2 *mm* high). This framework was based on
793 calculations of intracellular microscopic dipoles from a mathematical model for PCs in
794 the CA3 region (Traub et al. 1991). Using this framework, these authors were able to
795 reproduce changes in the magnetic field waveforms/amplitudes on a mesoscopic scale (i.e.
796 MEG detection coils were 2 *mm* from the slice) induced by a variety of pharmacological
797 manipulations. Based on equivalent ideas, biophysical models for mesoscopic regions in
798 the neocortex have been used latterly to explain large-scale electrophysiological data
799 (Murakami and Okada 2006; Jones et al. 2007, 2009). Recently, Riera et al. (2006)
800 proposed a simple way to include effective electrotonic resistive and capacitive ratios in a
801 forward/generative EEG model based on a three compartment representation of the layer
802 V tufted PC. In this study, these authors suggested a very descriptive relationship
803 between this biophysical model and the dipolar current sources in the visual cortex of
804 humans (Riera et al. 2007). They hypothesized that when the stimulation frequency is
805 increased, the returning capacitive currents across the neuron membrane will start
806 showing a saturation phenomenon due to an existing limit for its time relaxation. This
807 phenomenon is appreciated from a frequency of stimulation above 4 *Hz*. In our study, the
808 dipolar contributions were significantly smaller in the 3 *Hz* stimulation condition for the
809 case of dipole fitting, while monopolar ones were larger for both types of inverse

solutions. Our findings are in agreement with Riera et al. (2006) hypothesis due to the fact that dipolar components could also be majorly determined by the response capability of the membrane capacitors, i.e. the more saturated is the membrane capacitor the smaller could be the dipolar contribution to the extracellular potentials.

On the other hand, by comparing equations (2b) and (3), we could erroneously judge the existence of a mathematical ambiguity. Fortunately, such is not the case given that $I(\vec{r},t)$ and $m(\vec{r},t)$ are magnitudes associated with different spatial scales. Inside the mesoscopic level, the volume sources can be written in terms of a continuous vector field of electric currents $\vec{j}_m^{\,p}$, i.e. $s=-\nabla\cdot\vec{j}_m^{\,p}$ (dimensions: $\vec{j}_m^{\,p}\sim\mu A/mm^2$). However, we have to be prudent while extending this concept to the macroscopic level. For example, the definition of a mesoscopic monopolar source at $\vec{r}_0$ implies that a positive electric current is spreading out in the radial direction from that location. Therefore, a mesoscopic vector current source is not defined at $\vec{r}_0$. Nunez and Srinivansan (2006, appendix K) discussed some related aspects. We believe multipolar moments at $\vec{r}_0$ in a mesoscopic sense will be better defined in terms of the respective equivalent magnitudes: $m(\vec{r},t)=m(t)\delta(\vec{r}-\vec{r}_0)$, $\mathbf{d}(\vec{r},t)=\mathbf{d}(t)\delta(\vec{r}-\vec{r}_0)$, and $\mathbf{Q}(\vec{r},t)=\mathbf{Q}(t)\delta(\vec{r}-\vec{r}_0)$.

**Futures remarks**

In this paper, we have found that current monopoles and quadrupoles constitute significant source components of the skull EEG in the barrel cortex of Wistar rats. Therefore, forward/generative models for EEG data observed from rodents must be generalized in the future to include multipolar current configurations for any mesoscopic region. Based on our results, we would like to suggest the following strategy to solve the EEG inverse problem in rodents:

- Obtain characteristic dynamic equations of the multipolar current sources in the cortical columns from biophysical models of the principal neurons. These models must be descriptive rather than exhaustive, but must take into account ionic diffusion mechanisms as discussed above and the relevant geometrical characteristics of neurons. However, statistical magnitudes (e.g. occurrence

probability of postsynaptic currents, neuronal firing rate) impacting on the states of these neuronal populations must be clearly represented.

- Estimate the mesoscopic monopolar, dipolar and quadrupolar current sources from large-scale EEG data by solving a generalized inverse problem that makes use of both the characteristic dynamic equations and specific forward/generative models for all these types of current sources. Due to the differences in EEG and MEG observation modalities in terms of their visibility to multipolar current sources, it would be recommendable to perform this step from concurrent EEG and MEG recordings.

- Estimate the microscopic volume sources $s(\vec{r},t)$ from the mesoscopic multipolar moments using equations (1). Finally, reconstruct the dynamics of the abovementioned statistical magnitudes from $s(\vec{r},t)$ using the characteristic dynamic equations.

Finally, the existence of monopolar current sources in the neocortex of mammals would make a difference while comparing EEG and MEG data, since this type of current source would have no effect on the magnetic field. In our view, the existence of monopoles could give an alternative explanation to the large differences found in the EEG and MEG waveforms associated with interictal spike activity in a variety of epileptic patients (Huiskamp et al. 2004; Fernandes et al. 2005), a phenomenon difficult to explain with a single dipolar source under the quasi-static approach for the Maxwell equations. At this moment, alternative hypotheses for such waveform discrepancies are: **a**) the spatio-temporally distributed nature of these sources (Huiskamp et al. 2004) and **b**) the differences in the orientations of the underlying dipolar source (Fernandes et al. 2005).

## *Acknowledgement*

We would like to thank Prof. Ed X. Wu from the University of Hong Kong for helping us to establish suitable parameters for the acquisition of T1-weighted anatomical images. This work has been supported by the Japan-Canada Joint Health Research Program (JSPS) “The neuroarchitectonic determinants of EEG recordings”, the JSPS Grants-in-Aid (B) 18320062 and the JSPS Grant-in-Aid for Young Scientists (B) 23700492.

# References


**Abraham K, Ajmone-Marsan C.** Patterns of cortical discharges and their relation to routine scalp electroencephalography. *Electroenceph Clin Neurophysiol* 10: 447-461, 1958.

**Adrian ED, Matthews BHC.** The Berger rhythm: Potential changes from the occipital lobes in man. *Brain* 57(4): 355-385, 1934.

**Ahrens KF, Kleinfeld D.** Current flow in vibrissa motor cortex can phase-lock with exploratory rhythmic whisking in Rat. *J Neurophysiol* 92: 1700-1707, 2004.

**Baillet S, Mosher JC, Leahy RM.** Electromagnetic brain mapping. *IEEE Signal Processing Magazine*, November: 14-30, 2001.

**Bédard C, Destexhe A.** Macroscopic models of local field potentials and the apparent 1/f noise in brain activity. *Biophys. J* 96: 2589-2603, 2009.

**Beevers CA.** On the interpretation of electroencephalic potentials. *Edinburgh Roy Soc Proc* 62B: 43-50, 1944-7.

**Bereshpolova Y, Amitai Y, Gusev AG, Stoelzel CR, Swadlow HA.** Dendritic backpropagation and the state of the awake neocortex. *J. Neurosci*., 27: 9392-9399, 2007.

**Berger H.** Über das Elektroenkephalogramm des Menschen. *Archiv für Psychiatrie und Nervenkrankheiten* 87: 527-570, 1929.

**Bertrand O, Perrin F, Pernier J.** A theoretical justification of the average reference in topographic evoked potential studies. *Electroencephalogr Clin Neurophysiol* 62(6): 462-464, 1985.

**Boorman L, Kennerley AN, Johnston D, Jones M, Zheng Y, Redgrave P, Berwick J.** Negative blood oxygen level dependence in the rat: A model for investigating the role of suppression in neurovascular coupling. *J. Neurosci*., 30: 4285-4294, 2010.

**Bowyer SM, Okada YC, Papuashvili N, Moran JE, Barkley GL, Welch KMA, Tepley N.** Analysis of MEG signals of spreading cortical depression with propagation constrained to a rectangular cortical strip I. Lissencephalic rabbit model. Brain Research 843: 71-78, 1999.

**Brankačk J, Stewart M, Fox SE.** Current source density analysis of the hippocampal theta rhythm: associated sustained potentials and candidate synaptic generators. *Brain*

*Research* 615: 310-327, 1993.

**Brazier MAB.** The electrical fields at the surface of the head during sleep. *Electroencephalogr Clin Neurophysiol* l: 195-204, 1949.

**Buzsáki G, Kandel A.** Somadendritic backpropagation of action potentials in cortical pyramidal cells of the awake rat. *J Neurophysiol* 79: 1587-1591, 1998.

**Calvet J., Scherrer J.** Activité bioélectrique de l'écorce cérébrale á ses différents niveaux. *CR Soc Biol (Paris)*, 155: 275-278, 1961.

**Calvet J, Calvet MC, Scherrer J.** Étude stratigraphique corticale de l'activité: EEG spontanée. *Electroenceph Clin Neurophysiol* 17: 109-125, 1964.

**Chapman RM, Ilmoniemi RJ, Barbanera S, Romani GL.** Selective localization of alpha brain activity with neuromagnetic measurements. *Electroencephal Clin Neurophysiol* 58: 569-572, 1984.

**Cohen D, Cuffin BN.** Demonstrations of useful differences between magnetoencephalogram and electroencephalogram. *Electroenceph Clin Neurophysiol* 56: 38-51, 1983.

**Cooper R, Winter A.L., Crow H.J., Grey Walter W.** Comparison of subcortical, cortical and scalp activity using chronically indwelling electrodes in man. *Electroenceph Clin Neurophysiol* 18: 217-228, 1965.

**de Celis Alonso B, Lowe AS, Dear JP, Lee KC, Williams SCR, Finnerty GT.** Sensory inputs from whisking movements modify cortical whisker maps visualized with functional magnetic resonance imaging. *Cereb Cortex* 18: 1314-1325, 2008.

**Dehghani N, Bédard C, Cash SS, Halgren E, Destexhe A.** Comparative power spectral analysis of simultaneous electroencephalographic and magnetoencephalographic recordings in humans suggests non-resistive extracellular media. *J Computat Neurosci* 29: 405-421, 2011.

**de Munck JC, van Dijk BW.** Symmetry considerations in the quasi-static approximation of volume conductor theory. *Phys Med Biol* 36(4): 521-529, 1991.

**Di S, Baumgartner C, Barth D.** Laminar analysis of the extracellular field potentials in rat vibrissa/barrel cortex. *J Neurophysiol* 63: 832-840, 1990.

**Ebersole JS.** Defining epileptogenic foci: past, present, future. *J Clin Neurophysiol* 14: 470-483, 1997.

**Ebersole JS.** Noninvasive localization of epileptogenic foci by EEG source modeling. *Epilepsia* 41: S24–S33, 2000.

**Ferezou I, Haiss F, Gentet LJ, Aronoff R, Weber B, Petersen CCH.** Spatiotemporal dynamics of cortical sensorimotor integration in behaving mice. *Neuron* 56: 907-923, 2007.

**Fernandes JM, Martins da Silva A, Huiskamp G, Velis DN, Manshanden I, de Munck JC, Lopes da Silva F, Silva Cunha JP.** What does an epileptiform spike look like in MEG? Comparison between coincident EEG and MEG spikes. *J Clin Neurophysiol* 22: 68-73, 2005.

**Freeman WJ.** Distribution in time and space of prepyriform electrical activity. *J Neurophysiol* 22(6): 644-665, 1959.

**Freeman WJ.** Mass action in the nervous system. Academic Press, New York, 1975 (page 454).

**Gabriel S, Lau RW, Gabriel C.** The dielectric properties of biological tissues: II. Measurements in the frequency range 10 Hz to 20 GHz. *Phys Med Biol* 41: 2251-2269, 1996.

**Gabriel C, Peyman A, Grant EH.** Electrical conductivity of tissue at frequencies below1 MHz. *Phys Med Biol* 54: 4863-4878, 2009.

**Giebisch G, Tosteson DC, Ussing HH, Tosteson MT**. Membrane transport in biology. I- Concepts and models. *Springer-Verlag Berlin Heidelberg New York*, 1978.

**Gold C, Henze DA, Koch C, Buzsáki G.** On the origin of the extracellular action potential waveform: a modeling study. *J Neurophysiol* 95: 3113-3128, 2006.

**Gold C, Henze DA, Koch C.** Using extracellular action potential recordings to constrain compartmental models. *J Comput Neurosci* 23: 39-58, 2007.

**Goto T, Hatanaka R, Ogawa T, Sumiyoshi A, Riera J, Kawashima R.** An evaluation of the conductivity profile in the barrel cortex of Wistar rats. *J Neurophysiol* 104: 3388-3412, 2010.

**Goto T, Riera J, Kawashima R.** An electrophysiological microscope for fast assessments to the activity of cortical networks in vivo: from population inputs to single unit outputs. *Nature Methods*, submitted, 2012.

**Grochowski P, Trylska J.** Continuum molecular electrostatics, salt effects, and

counterion binding-A review of the Poisson-Boltzmann theory and its modifications. *Biopolymers* 89: 93-113, 2007.

**Gumnit R, Takahashi T.** Changes in direct current activity during experimental focal seizures. *Electroencephalogr Clin Neurophysiol* 19: 63-74, 1965.

**Hämäläinen M, Ilmoniemi R.** Interpreting measured magnetic fields of the brain: estimates of current distributions. *Report TKK-F-A559*, Helsinki University of Technology, Espoo, Finland, 1984.

**Hämäläinen MS, Sarvas J.** Realistic conductivity geometry model of the human head for interpretation of neuromagnetic data. *IEEE Trans Biomed Eng* 36: 165-171, 1989.

**Hämäläinen M, Hari R, Ilmoniemi R, Knuutila J, Lounasmaa O.** Magnetoencephalography. Theory, instrumentation and applications to the noninvasive study of human brain function. *Rev Mod Phys* 65: 413-497, 1993.

**Hari R, Ilmoniemi R.** Cerebral magnetic fields. *CRC Critical Reviews in Biomedical Engineering* 14(2): 93-126, 1986.

**Henderson CJ, Butler SR, Glass A.** The localization of equivalent dipoles of EEG sources by the application of electrical field theory. *Electroenceph Clin Neurophysiol* 39: 117-130, 1975.

**Higley MJ, Contreras D.** Cellular mechanisms of suppressive interactions between somatosensory responses in vivo. *J Neurophysiol* 97: 647-658, 2007.

**Holt GR, Koch C.** Electrical Interactions via the Extracellular Potential Near Cell Bodies *J Comput Neurosci* 6, 169-184, 1999.

**Huiskamp G, van der Meij W, van Huffelen A, van Nieuwenhuizen O.** High resolution spatio-temporal EEG-MEG analysis of Rolandic spikes. *J Clin Neurophysiol* 21: 84-95, 2004.

**Humphrey DR.** Re-analysis of the antidromic cortical response. I. Potentials evoked by stimulation of the isolated pyramidal tract. *Electroenceph Clin Neurophysiol* 24: 116-129*,* 1968.

**Jerbi K, Mosher JC, Baillet S, Leahy RM.** On MEG forward modelling using multipolar expansions. *Phys Med Biol* 47: 523-555, 2002.

**Johnston D**, **Wu SM-S**. Foundations of cellular neurophysiology. Bradford Books, 1st edition, 1994.

**Jones SR, Pritchett DL, Stufflebeam SM, Hämäläinen M, Moore CI.** Neural correlates of tactile detection: a combined magnetoencephalography and biophysically based computational modeling study. *J. Neurosci.* 27: 10751-10764, 2007.

**Jones SR, Pritchett DL, Sikora MA, Stufflebeam SM, Hämäläinen M, Moore CI.** Quantitative analysis and biophysically realistic neural modeling of the MEG mu rhythm: rhythmogenesis and modulation of sensory-evoked responses. *J. Neurophysiol* 102: 3554-3572, 2009.

**Kennedy JL, Gottsdanker RM, Armington JC, Gray FE.** A new electroencephalogram associated with thinking. *Science* 108: 527-529, 1948.

**Klee M, Rall W.** Computed potentials of cortically arranged populations of neurons. *J Neurophysiol* 40: 647-666, 1977.

**Kraut MA, Arezzo JC, Vaughan HG.** Intracortical generators of the flash VEP in monkeys. *Electroenceph Clin Neurophysiol* 62: 300-312, 1985.

**Lakatos P, Chen C-M, O'Connell MN, Mills A, Schroeder CE.** Neuronal Oscillations and Multisensory Interaction in Primary Auditory Cortex. *Neuron* 53: 279-292, 2007.

**Lakatos P, Karmos G, Mehta AD, Ulbert I, Schroeder CE.** Entrainment of neuronal oscillations as a mechanism of attentional selection. *Science* 320: 110-113, 2008.

**Li CL, Bak AF, Parker LO.** Specific resistivity of the cerebral cortex and white matter. *Exp Neurol* 20: 544-557, 1968.

**Li B.** Continuum electrostatics for ionic solutions with non-uniform ionic sizes. *Nonlinearity* 22: 811-833, 2009.

**Llinás RR Nicholson C.** Analysis of field potential in the central nervous system. *Handbook of Electroencephalogr Clin. Neurophysiol.* 2B: 61-84, 1974.

**Lopes da Silva FH, Van Leeuwen WS.** The cortical source of the alpha rhythm. *Neuroscience Letters* 6: 237-241, 1977.

**Lorente de No R.** Analysis of the distribution of the action currents of nerve in volume conductors. *Stud Rockefeller Inst Med Res* 132, 384-477, 1947.

**Malmivuo J, Plonsey R.** Bioelectromagnetism. Principles and applications of bioelectric and biomagnetic fields. *Oxford University Press*, 1995.

**Mégevand P, Quairiaux C, Lascano AM, Kiss JZ, Michel CM.** A mouse model for

studying large-scale neuronal networks using EEG mapping techniques. *Neuroimage* 42: 591-602, 2008.

**Mikuni N, Nagamine T, Ikeda A, Terada K, Taki W, Kimura J, Kikuchi H. Shibasaki H.** Simultaneous recording of epileptiform discharges by MEG and subdural electrodes in temporal lobe epilepsy. *Neuroimage* 5: 298-306, 1997.

**Milstein JN, Koch C.** Dynamic moment analysis of the extracellular electric field of a biologically realistic spiking neuron. *Neural Computation* 20: 2070-2084, 2008.

**Mosher JC, Lewis PS, Leahy RM.** Multiple dipole modeling and localization from spatio-temporal MEG data. *IEEE Trans Biomed Eng* 39(6): 541-557, 1992.

**Murakami S, Zhang T, Hirose A, Okada YC.** Physiological origins of evoked magnetic fields and extracellular field potentials produced by guinea-pig CA3 hippocampal slices. *J. Physiol. (Lond.)* 544: 237-251, 2002.

**Murakami S, Okada Y.** Contributions of principal neocortical neurons to magnetoencephalography and electroencephalography signals. *J. Physiol. (Lond.)* 575: 925-936, 2006.

**Niedermeyer E, Lopes da Silva F.** *Electroencephalography: Basic principles-clinical applications and related fields (2nd ed.)*. Baltimore: Urban & Schwarzenberg, 1987.

**Nunez PL**. *Electric Fields of the Brain.* Oxford: New York, 1981.

**Nunez P, Srinivasan R.** *Electric fields of the brain. The neurophysics of EEG*, Second edition. Oxford University Press: USA, 2006.

**Ogawa T, Riera J, Goto T, Sumiyoshi A, Nonaka H, Jerbi K, Bertrand O, Kawashima R.** Large-scale heterogeneous representation of sound attributes in rat primary auditory cortex: From unit activity to population dynamics. *J Neurosci* 31(41): 14639-14653, 2011.

**Oishi M, Otsubo H, Kameyama S, Morota N, Masuda H, Kitayama M, Tanaka R.** Epileptic spikes: magnetoencephalography versus simultaneous electrocorticography. *Epilepsia* 43: 1390-1395, 2002.

**Okada YC, Wu J, Kyuhou S.** Genesis of MEG signals in a mammalian CNS structure. *Electroencephalogr Clin Neurophysiol* 103: 474-485, 1997.

**Oostendorp T, Delbeke J, Stegeman DF.** The conductivity of human skull: results of in vivo and in vitro measurements. *IEEE Trans Biomed Eng* 47: 1487-1492, 2000.

**Pascual-Marqui RD.** Review of methods for solving the EEG inverse problem. *Int J Bioelectromagnetism* 1(1): 75-86, 1999.

**Paxinos G, Watson C.** *The rat brain in stereotaxic coordinates, Sixth edition.* Academic Press, Elsevier: Burlington. 2007.

**Petersen CCH.** The functional organization of the barrel cortex. *Neuron* 56: 339-355, 2007.

**Petsche H, Prohaska O, Rappelsberger P, Vollmer R, Pockberger H.** Simultaneous laminar intracortical recordings in seizures. *Electroenceph Clin Neurophysiol* 42: 414-416, 1977.

**Pettersen K, Devor A, Ulbert I, Dale AM, Einevoll GT.** Current-source density estimation based on inversion of electrostatic forward solution: Effects of finite extent of neuronal activity and conductivity discontinuities. *J Neurosci Methods* 154: 116-133, 2006.

**Pettersen KH, Einevoll GT.** Amplitude variability and extracellular low-pass filtering of neuronal spikes. *Biophysical Journal* 94: 784-802, 2008.

**Plonsey R.** *Bioelectric phenomena.* New York: McGraw-Hill, 1969.

**Plonsey R**, **Heppner DB**. Considerations of quasi-stationarity in electrophysiological systems. *Bull Math Biophys* 29(4):657-664, 1967.

**Pollen DA.** On the generation of neocortical potentials. In: H.H. Jasper, A.A. Ward and A. Pope (Eds.), Basic Mechanisms of the Epilepsies. Little, Brown and Co., Boston, MA, 1969 (pages 411-420).

**Rall W.** Electrophysiology of a dendritic neuron model. Biophys J 2: 145-167, 1962.

**Ranck JB Jr.** Specific impedance of rabbit cerebral cortex. *Exp Neurol* 7: 144-152, 1963.

**Rappelsberger P, Pockberger H, Petsche H.** The contribution of the cortical layers to the generation of the EEG field potential and current source density analyses in the rabbit's visual cortex. *Electroenceph Clin Neurophysiol* 53: 254-269, 1982.

**Riera JJ, Aubert E, Valdes-Sosa P, Casanova R, Lins O.** *Discrete spline electric-magnetic tomography (DSPECT) based on realistic neuroanatomy*. In Biomag 96. Proceedings of the Tenth International Conference on Biomagnetism, Springer-Verlag: New York, 326-329, 2000.

**Riera JJ, Wan X, Jimenez JC, Kawashima R.** Nonlinear local electro-vascular

coupling. Part I: A theoretical model. *Hum Brain Mapp* 27: 896-914, 2006.

**Riera JJ, Jimenez JC, Wan X, Kawashima R, Ozaki T.** Nonlinear local electro-vascular coupling. Part II: From data to neural masses. *Hum Brain Mapp* 28: 335-354, 2007.

**Riera JJ, Schousboe A, Waagepetersen HS, Howarth C, Hyder F.** The micro-architecture of the cerebral cortex: Functional neuroimaging models and metabolism. *NeuroImage* 40: 1436-1459, 2008.

**Riera J, Ogawa T, Hatanaka R, Goto T, Sumiyoshi A, Enjieu-Kadji H, Nakauchi S, Kawashima R.** Concurrent observations of astrocytic $Ca^{2+}$ activity and multi-site extracellular potentials from an intact cerebral cortex. *J Biophotonics* 3: 147-160, 2010a.

**Riera JJ, Sumiyoshi A, Kawashima R.** *MRI compatible mini-cap for EEG recordings from rodents.* Patent Application Number: JP 2010-983220, Japan, 2010b.

**Scherg M, Von Cramon D.** Two bilateral sources of the late AEP as identified by a spatio-temporal dipole model. *Electroencephalogr Clin Neurophysiol* 62(1): 32-44, 1985.

**Schneider MR.** A multistage process for computing virtual dipolar sources of EEG discharges from surface information. *IEEE Trans Biomed Eng* BME-19: 1-12, 1972.

**Sem-Jacobsen CW, Petersen MC, Lazarte JA, Dodge HW, Holman CB.** Electroencephalographic rhythms from depths of the frontal lobe in 60 psychotic patients. *Electroenceph Clin Neurophysiol* 7: 193-210, 1955.

**Shaw JC, Roth M.** Potential distribution analysis. II: A theoretical consideration of its significance in terms of electric field theory. *Electroenceph Clin Neurophysiol* 7: 285-292, 1955.

**Shu Y, Hasenstaub A, Duque A, Yu Y, McCormick DA.** Modulation of intracortical synaptic potentials by presynaptic somatic membrane potential. *Nature* 441: 761-765, 2006.

**Sumiyoshi A, Riera JJ, Ogawa T, Kawashima R.** A mini-cap for simultaneous EEG and fMRI recording in rodents. *Neuroimage* 54: 1951-1965, 2011.

**Tao JX, Ray A, Hawes-Ebersole S, Ebersole JS.** Intracranial EEG substrates of scalp EEG interictal spikes. *Epilepsia* 46: 669-676, 2005.

**Traub RD, Wong RKS, Miles R, Michelson H.** A model of a CA3 hippocampal pyramidal neuron incorporating voltage-clamp data on intrinsic conductances. *J. Neurophysiol* 66: 635-650, 1991.

**Walter WG, Walter VJ.** The electrical activity of the brain. *Annu Rev Physiol* 11: 199-230, 1949.

**Xu XL, Xu B, He B.** An alternative subspace approach to EEG dipole source localization. *Phys Med Biol* 49(2): 327-343, 2004.

**Zheng Q, Wei G-W.** Poisson–Boltzmann–Nernst–Planck model. *J Chem Phys* 134, 194101, 2011.

## Appendix I

**A:** *The spatiotemporal filtering properties of the cortical tissues*

In brain tissues with multiple and non-instantaneous dielectric relaxation mechanisms, the constitutive relationships depend in a very particular way on the frequency within specific ranges. Also, as a consequence of the existence of complex microscopic structures in the brain tissues both conductivity and permittivity could depend on location (i.e. local inhomogeneities) and orientation (i.e. local anisotropies). For example, the existence of significant ionic diffusion might indirectly affect the electric permittivity $\vec{\varepsilon}(\vec{r},\omega)$ due to counterion polarizations at low frequencies $\omega$.

$$\vec{\mathbf{D}}(\vec{r},t) = \int_{-\infty}^{\infty} \vec{\varepsilon}(\vec{r},\tau)\vec{\mathbf{E}}(\vec{r},\tau)\,d\tau \qquad \text{(A-1a)}$$

$$\vec{\mathbf{J}}_{Ohm}(\vec{r},t) = \int_{-\infty}^{\infty} \vec{\sigma}(\vec{r},\tau)\vec{\mathbf{E}}(\vec{r},\tau)\,d\tau \qquad \text{(A-1b)}$$

In other words, $\vec{\mathbf{J}}_{Ohm}(\vec{r},\omega) = \vec{\sigma}(\vec{r},\omega)\vec{\mathbf{E}}(\vec{r},\omega)$ and $\vec{\mathbf{D}}(\vec{r},\omega) = \vec{\varepsilon}(\vec{r},\omega)\vec{\mathbf{E}}(\vec{r},\omega)$ . The magnitude $\vec{\mathbf{D}}(\vec{r},\omega)$ represents the electric displacement and $\vec{\varepsilon}(\vec{r},\omega)$ is the permittivity tensor for brain tissues. The equations (A-1) imply that any mesoscopic volume inside the brain (e.g. a barrel) behaves like a multiple spatial filtering device with frequency characteristics depending notably on location and orientation. Bearing in mind that the maximum sampling rate used for standard LFP observation is about 500 *Hz*, one must be careful while assuming that any ideal closed-loop inside the tissue can be locally modeled as an ideal RC circuit. In such an imaginary loop, the total electric current in a particular region (A) may be smaller than in an adjacent region (B) within a particular frequency range $\omega_L$ (Fig. I-A, i.e. $I_{A\to B}(\omega_L) << I_{B\to A}(\omega_L)$).

Thus, even though the actual total ohmic current, from where our LFP observations originate, is conserved within the loop and directly related to the impressed currents in each tissue region, for the observable frequency range it may apparently look like there are virtual either sources or sinks of electric current along the loop over time.

$$I^{Total}_{\substack{A\to B \\ B\to A}} = I^{\text{Impressed}}_{A} + I^{\text{Impressed}}_{B}$$

**B:** *The ionic diffusion phenomenon*

As mentioned in the main text, the total electric current inside any mesoscopic brain area has usually been represented as the superposition of non-dispersive ohmic electric currents $\vec{\mathbf{J}}_{Ohm}(\vec{r},t)=\vec{\sigma}(\vec{r})\vec{\mathbf{E}}(\vec{r},t)$ and certain fictitious current sources $\vec{\mathbf{J}}_{P}(\vec{r},t)$ that we name impressed. Hence, we ignore any contribution from ionic diffusion currents (Bédard and Destexhe 2009). Additionally, the actual biophysical origin of $\vec{\mathbf{J}}_{P}(\vec{r},t)$ is a set of trans-membrane currents that results from temporal changes in the membrane permeability to certain ions, i.e. $\vec{\mathbf{J}}_{P}(\vec{r},t)$ is created from strong electrochemical gradients across the cellular membranes.

Therefore, to have a proper formalization of the electrophysiological forward problem, it is necessary to have a term $\vec{\mathbf{J}}_{Diff}(\vec{r},t)$ explicitly describing the diffusion of a variety of ions (B-1) typically of different sizes (Li 2009). In this context, the impressed current source $\vec{\mathbf{J}}_{P}(\vec{r},t)$ might irreversibly result from these ohmic and ionic diffusion currents in situations of thermodynamic disequilibrium.

$$\vec{\mathbf{J}}_{Total}(\vec{r},t)=\vec{\mathbf{J}}_{Ohm}(\vec{r},t)+\vec{\mathbf{J}}_{Diff}(\vec{r},t) \qquad \text{(B-1)}$$

The total ionic diffusion current is defined as $\vec{\mathbf{J}}_{Diff}(\vec{r},t)=\sum_{\mathbf{i}} Fz_i\vec{\mathbf{f}}_i(\vec{r},t)$, with the flux for each ion species given by the Fick's first law, i.e. $\vec{\mathbf{f}}_i(\vec{r},t)=-\vec{D}_i(\vec{r})\nabla c_i(\vec{r},t)$ (Malmivuo and Plonsey 1995). The diffusion coefficient tensor $\vec{D}_i(\vec{r})=\vec{u}_i(\vec{r})RT/|z_i|F$ for each ion depends linearly on its mobility $\vec{u}_i(\vec{r})$ (i.e. *the Einstein–Smoluchowski relation*). The ion charge number, temperature and gas constant are represented here by symbols $z_i$, $T$ and $R$, respectively.

Under the conditions that the ions do not interact and that their concentrations are sufficiently low, the mesoscopic Maxwell equations for the propagation of the electromagnetic field in an electrolyte are:

For the electric $\vec{\mathbf{E}}(\vec{r},t)$ and displacement $\vec{\mathbf{D}}(\vec{r},t)$ fields

$$\nabla\cdot\vec{\mathbf{D}}(\vec{r},t)=\rho_{Total}(\vec{r},t) \qquad \textit{Gauss's law} \qquad \text{(B-2a)}$$

$$\nabla \times \vec{\mathbf{E}}(\vec{r},t) = -\frac{\partial \vec{\mathbf{B}}(\vec{r},t)}{\partial t} \qquad \textit{Faraday's law of induction} \qquad \text{(B-2b)}$$

For the magnetic flux density $\vec{\mathbf{B}}(\vec{r},t)$

$$\nabla \cdot \vec{\mathbf{B}}(\vec{r},t) = 0 \qquad \rightarrow \qquad \vec{\mathbf{B}}(\vec{r},t) = \nabla \times \vec{\mathbf{A}}(\vec{r},t) \qquad \text{(B-2c)}$$

$$\frac{\nabla \times \vec{\mathbf{B}}(\vec{r},t)}{\mu_0} = \vec{\mathbf{J}}_{Total}(\vec{r},t) + \frac{\partial \vec{\mathbf{D}}(\vec{r},t)}{\partial t} \qquad \textit{Ampere's law} \qquad \text{(B-2d)}$$

The magnitude $\vec{\mathbf{A}}(\vec{r},t)$ is named the magnetic vector potential. At the frequency range of the electrophysiological phenomena, any magnetization of brain tissues has been historically ignored.

In order to warrant the conservation of the total charge $\nabla \cdot \vec{\mathbf{J}}_{Total}(\vec{r},t) + \partial \rho_{Total}(\vec{r},t)/\partial t = 0$ whenever ionic diffusion processes are present, the Poison's law must include a term that describes ionic charge re-distributions. The resulting Maxwell's equation (B-2a) is known as the Poisson-Boltzmann's law (Grochowski and Trylska 2007). By definition, the total charge density comprises a free and an ionic diffusion component, i.e., $\rho_{Total}(\vec{r},t) = \rho_{Free}(\vec{r},t) + \rho_{Ion}(\vec{r},t)$, with $\rho_{Ion}(\vec{r},t) = \sum_i F z_i c_i(\vec{r},t)$. Henceforth, let us consider for simplicity only the case of media both isotropic and with a single/instantaneous dielectric relaxation mechanism, i.e. $\vec{\mathbf{D}}(\vec{r},t) = \varepsilon(\vec{r})\vec{\mathbf{E}}(\vec{r},t)$ and $\vec{\mathbf{J}}_{Ohm}(\vec{r},t) = \sigma(\vec{r})\vec{\mathbf{E}}(\vec{r},t)$. Also, we are not interested on cases where a free charge density is created by particular distributions of macromolecules, i.e. we assume the free charge density is zero inside brain tissues.

Under a quasi-static approach (Plonsey and Heppner 1967; de Munck and van Dijk 1991), there are two main hypotheses about the propagation of electromagnetic field in biological tissues at low frequencies ( $\omega \leq 10\,kHz$ ), which are based on mean values (Hämäläinen 1993; Nunez et al. 2006) of the electric conductivity $\bar{\sigma} \approx 0.3\,S/m$ and permittivity $\bar{\varepsilon} \approx 10^5\,\varepsilon_0$. The first hypothesis results from comparing the size of the mammalian head and the characteristic length $\lambda = \left[\mu_0 \omega^2 \bar{\varepsilon}\left(1 - i\bar{\sigma}/\omega\bar{\varepsilon}\right)\right]^{-1/2} \approx 65\,m$ of the electromagnetic propagation wave. Consequently, any Faraday's induction effect is disregarded, i.e. $\nabla \times \vec{\mathbf{E}}(\vec{r},t) = 0$, and the electric field is represented as a gradient of an

electric potential $\vec{\mathbf{E}}(\vec{r},t)=-\nabla\varphi(\vec{r},t)$. At any location inside the brain, the displacement current is much smaller than the ohmic current, e.g. $(1+i\omega\bar{\varepsilon}/\bar{\sigma})\approx 1$, which constitutes the second hypothesis of the quasi-static approach. Therefore, the mesoscopic Maxwell equations for such a particular case are:

$$-\nabla\cdot\left(\varepsilon(\vec{r})\nabla\varphi(\vec{r},t)\right)=\sum_i Fz_i c_i(\vec{r},t) \tag{B-3a}$$

$$\frac{\nabla\times\nabla\times\vec{\mathbf{A}}(\vec{r},t)}{\mu_0}=-\sigma(\vec{r})\nabla\varphi(\vec{r},t)-\sum_i Fz_i D_i(\vec{r})\nabla c_i(\vec{r},t) \tag{B-3b}$$

On the other hand, as a consequence of electrochemical gradients $\mu_i(\vec{r},t)$ in the brain tissues, the total ionic flux for each species is determined by the sum of diffusion and electrical current components.

$$\vec{\mathbf{j}}_i(\vec{r},t)=-\frac{D_i(\vec{r})c_i(\vec{r},t)}{RT}\nabla\mu_i(\vec{r},t) \tag{B-4}$$

$$\mu_i(\vec{r},t)=\mu_i^0+RT\log\left(c_i(\vec{r},t)\right)+Fz_i\varphi(\vec{r},t) \tag{B-5}$$

Based on the mass conservation law for each ion, i.e. $\nabla\cdot\vec{\mathbf{j}}_i(\vec{r},t)=-\frac{\partial c_i(\vec{r},t)}{\partial t}$, its concentration in the tissue must obey the following equation:

$$\frac{\partial c_i(\vec{r},t)}{\partial t}=\nabla\cdot\left[D_i(\vec{r})\left(\nabla c_i(\vec{r},t)+\frac{Fz_i c_i(\vec{r},t)}{RT}\nabla\varphi(\vec{r},t)\right)\right] \tag{B-6}$$

Equations (B-3a) and (B-6) together constitute the classical Poisson-Boltzmann-Nernst-Planck model (Zheng and Wei 2011).

Let us assume that, as a result of the neuronal activity, there are timely changes in the trans-membrane mobility to certain ions $u_i(\vec{r})$. These changes will cause the emergence of impressed current sources $\vec{\mathbf{J}}_P(\vec{r},t)=\sum_{i\in\Theta} Fz_i\vec{\mathbf{j}}_i(\vec{r},t)$, which might include both ohmic and ionic diffusion components.

$$\frac{\partial c_i(\vec{r},t)}{\partial t}=\nabla\cdot\left[D_i(\vec{r})\left(\nabla c_i(\vec{r},t)+\frac{Fz_i c_i(\vec{r},t)}{RT}\nabla\varphi(\vec{r},t)\right)\right]-\nabla\cdot\vec{\mathbf{j}}_i(\vec{r},t) \qquad i\in\Theta \tag{B-7a}$$

$$\frac{\nabla\times\nabla\times\vec{\mathbf{A}}(\vec{r},t)}{\mu_0}=-\sigma(\vec{r})\nabla\varphi(\vec{r},t)+\sum_i Fz_i D_i(\vec{r})\nabla c_i(\vec{r},t)+\vec{\mathbf{J}}_P(\vec{r},t) \tag{B-7b}$$

Under the validity of the Nernst-Planck electroneutrality condition, equations B-7a and B-7b are equivalent, with the total conductivity $\sigma(\vec{r}) = \sum_i F z_i u_i(\vec{r}) \hat{c}_i(\vec{r})$ defined from mean values $\hat{c}_i(\vec{r})$ of the ion concentrations over time (Giebish et al. 1978).

The cause-effect flow diagram for the general system of equations, i.e., (B-3a) and (B-7), is shown in figure I-B.

*Insert figure I around here*

# Figure Legends

**Figure 1.** The three-dimensional probe and the EEG mini-cap. **A-** The customized design of the three-dimensional probe (a courtesy from NeuroNexus). A picture of the three-dimensional probe taken just before insertion in the somatosensory barrel cortex with a digital microscope (KH-1300, HIROX, Tokyo). **B-** A view from the bottom of the EEG mini-cap is shown. The EEG mini-cap is created from melted plastic poured into a mold. In the mold made from plaster, stainless steel needles were perpendicularly situated in those positions defined for the electrodes. The needles were covered with hard plastic tubes (1.5 *mm*) which were finally fixed to the melted plastic. A hole was created for intracranial LFP recording (Probe Area). Three aluminum bars were also fused with the plastic. These aluminum bars are needed to firmly attach the EEG mini-cap to the skull. The EEG mini-cap has sliding silicon tubes (1.4 *mm*) positioned inside the hard plastic tubes. The silicon tubes, which are filled with a conductive gel, contain platinum wires. The actual impedance values of the EEG electrodes for this particular experiment, as determined by the *BrainVision Recorder* software (Brain Products GmbH), are shown using color coding (*bottom panel*).

**Figure 2.** The multipolar current sources for unit activity of principal cortical neurons. **A-** The overlapping of action potentials generated by ten layer V tufted PCs (grey dashed-lines) is shown on the top-left panel. The mean of the action potentials is highlighted (black continuous-line). On the top-right panel, we display the spatial distribution of the volumetric CSD generated by this cell type at the time instant of largest negativity in their action potentials (i.e. black arrow), which clearly shows a bipolar shape. The CSD distributions are represented in three-dimensional contours. The contours denoted by meshes and patches represent the weak (30% of the maximum) and strong (70% of the maximum) intensity of the CSD, respectively. The time courses of the monopolar, dipolar and quadrupolar moments are shown on the bottom-left panels. The sum of the monopolar moment along the entire time window (i.e. 4 *ms*) was zero (green dashed-line).

For the dipolar and quadrupolar moments, we calculate at each time instant the norm of the corresponding vector and tensor (i.e. *the trace*), respectively. The multipolar moments were calculate with respect to the center of gravity of the layer V tufted PCs. For these

time series to be comparable, the multipolar moments must be standardized taking into account the actual length of this type of PCs. The dipolar moments generated by these PCs along the *x*, *y* and *z* directions at the time instant of maximal dipolar activity (i.e. brown-dashed-vertical line) are revealed in the bottom-right panel together with their respective standard deviations. **B**- Same panels as in (A), but for the layer IV SS cells (ten cells). **C**- A comparison between the intensity of the monopolar moment for layer V tufted PC and layer IV SS cells at the time instant of largest negativity in their respective action potentials, i.e. black arrows in (A) and (B), respectively.

**Figure 3.** A volumetric CSD analysis from LFP recorded during single whisker deflections. **Top-left panel:** The grand-average CSD spatiotemporal map obtained from averaging the x-y projections of the volume sources *s* over all rats. These projections were obtained by pooling *s* along the x-y directions within each particular activated barrel. The black-dashed-vertical line indicates the time instant for the whisker deflections. The relative positions of the layer V tufted PC is presented. **Top-right panel:** The combined cytochrome C oxidase and DiI histological images (a tangential section) showing the position of the three-dimensional probe respect to the barrel field. A particular barrel is highlighted in blue. **Bottom-left panel:** The means and standard deviations of the multipolar moments are shown. For each deflected whisker, the corresponding multipolar moments were calculated using eq. (1a) with the volume of interest defined as the actual anatomical barrel. For these magnitudes to be comparable, the dipolar and quadrupolar components must be divided by $l$ and $l^2$, respectively. In the case of the dipolar and quadrupolar current components, their respective norms were used. The cortical thickness $l$ in the barrel cortex was 2 *mm*. As in figure 2 (A and B), the sum of the monopolar moment along the entire time window (i.e. 200 *ms*) was zero (green dashed-line). **Bottom-right panel:** The dipolar components along the *x*, *y* and *z* directions at the time instant of maximal dipolar activity (i.e. brown-dashed-vertical line) is shown together with their respective standard deviations.

**Figure 4.** The mean and standard deviation of the monopolar moment generated by a 2.5 $m^3$-voxel during a whole whisker stimulation protocol is shown. The sum of the monopolar moment along the entire time window (i.e. 300 *ms*) was zero (green dashed-

line).

**Figure 5. A-** The histological analysis. A coronal section of the barrel cortex obtained from the postmortem fixed brain. The three color panels on the left represent the cytochrome C oxidase (brown), the Nissl body staining (cyan) and the trace produced by the shank after the insertion (red-orange). The cytochrome C oxidase immunostaining helps us to determine accurately the limits of layer IV, where barrels (cyan boxes) and septums (white inter-spaces) were clearly defined. In order to produce such a trace, a florescent lipophilic neuronal tracer was gently applied to the side of the probe (i.e. the side of the silicon in opposition to the microelectrode array). A long probe was used in this particular example. The cortical layer can be distinguished from the fluorescent Nissl images. Large PCs are mostly distributed around layers V and VI. The multicolor composed image is shown on the left, with a particular distinction to the laminar profile. **B-** A single trial CSD analysis. **Top:** The color maps representing the spatial distributions of LFPs in a section of the barrel cortex (0.5-1.1 *mm*) of a particular rat are shown (1 *Hz* – top, 3 *Hz* – bottom), The actual amplitudes (mV) of the LFPs are represented by a bar color coding. The relative position of the layer V tufted PC with respect to these maps is also illustrated. **Bottom:** The CSD analysis, performed with the iCSD method (Pettersen et al., 2006), from the LFP (**Top**) are shown in the left and right panels (1 *Hz* – top, 3 *Hz* – bottom), respectively. Even for this particular trial, data were not acquired for the very superficial layers (e.g. layer I), the iCSD method provided interpolated estimators of the volume sources in these layers under a boundary condition $s(z)\big|_{z=l} = 0$ on the pial surface.

**Figure 6.** The population CSD analysis. **Top panels:** The means by which the CSD single trials (all experimental data) were calculated by the iCSD method are shown (top – 1 *Hz* and bottom – 3 *Hz*). These means were calculated after co-registering the probes used in all experiments by means of the immunostaining images. The insertion depths of the probes were different from trial to trial, and defined in that way to cover the whole z-axis of a barrel field. In some cortical layers, the sink/source arrangements showed dipolar-like symmetries, but in others, more complex spatiotemporal patterns were obvious. The relative positions of the layer II/III PC and layer V tufted PC are also

exposed. In order to quantify the charge balance along cortical layers, the multipolar moments (eq. 1b) were calculated from the mean CSD. **Bottom panels:** The time courses of the monopolar, dipolar and quadrupolar moments are shown. The multipolar moments were calculated with respect to the center of gravity of the cerebral cortex (i.e. 1 *mm* depth). The use of the center of the charge produced time courses with no clear meanings. For comparison, these moments must be standardized taking into account the actual cortical thickness.

**Figure 7.** The event-related EEG signal. **A.** The event-related EEG signal are shown at the top (1 *Hz* and 3 *Hz* stimulus condition). Four main components (C1-C4) were clearly distinguished, which are probably related to the activation of the primary somatosensory/motor cortices. Their corresponding topographic maps on the skull are shown at the bottom, which reveal their much extended spatial patterns. The time instants for these components are marked with dashed vertical lines. **B.** The time course of the event-related EEG signal, with the respective standard deviation, for one particular electrode (#14, close to the barrel cortex) is shown. The inter-individual variability was small compared to the size of the event-related response.

**Figure 8.** The EEG inverse solution in the barrel field. The mean amplitudes of the equivalent current dipole $d(\vec{r},t)$ (i.e. $d_{IS}^{F}(t)$) for the barrel field are shown for both stimulus frequencies. This magnitude was estimated using the single dipole fitting strategy (upper panels) and the surface LORETA inverse solution (lower panels). The standard deviations are represented by dashed lines. The estimated dipole amplitudes revealed very consistent waveforms across all experiments.

**Figure 9.** The linear regression analysis. Comparison of the actual large-scale waveform $d_{IS}^{F}(t)$ (black line) resulting from each inverse solution and that reconstructed by the linear regression model (black-dotted line). The upper and lower panels show the comparison for dipole fitting and LORETA inverse solution, respectively. The left and right panels show results for 1 *Hz* and 3 *Hz* stimulation frequency, respectively. The large-scale waveforms $d_{IS}^{F}(t)$ were normalized to the minimum peak at 60 *ms* after stimulus onset, a characteristic that was very replicable for all inverse solutions and

stimulation frequencies.

**Figure 10.** A statistical comparison of the multipolar components. The contribution of monopole, dipole, and quadrupole to large-scale waveforms $d_{IS}^{F}(t)$ for different inverse solutions and stimulus conditions. The values of the linear regression coefficients $\chi_{L}^{\{IS,F\}}$ are presented in a bar-plotting style with the respective STD estimated using data from the nine rats. The coefficients for the monopolar components were significantly larger than those for the dipolar and quadrupolar ones (two-way ANOVA with multiple comparison, $p < 0.0001$).

**Figure I. A.** The schematic illustration of the first scenario for the CSD unbalance. A mesoscopic cortical region (i.e. a barrel) comprises two tissues, which could represent supra-granular (A) and infra-granular (B) layers. In the somatosensory cortex of rats, these layers have been found to have different conductivity values at 500 Hz (Goto et al. 2010). These tissues have additionally different spectral characteristics for the electric conductivity (left), with the particularity that, for example, tissue A is less conductive than tissue B for the frequency range of the LFP. The total impressed current generated by the neuronal activity in the A and B tissues are $I_{A}^{\text{Impressed}}$ and $I_{B}^{\text{Impressed}}$, respectively. These impressed currents generate a total electric current flowing along a closed loop, with $I_{A\to B}^{Total}$ and $I_{B\to A}^{Total}$ for the respective sectors in each tissue. From the Kirchhoff's current law, we must expect that $I_{A\to B}^{Total} = I_{B\to A}^{Total}$. However, the total ohmic current in each tissue separates into a component with low-frequency variations, which causes the LFP, and a non-observable component with high-frequency variations. Even though the total ohmic current may be conserved, the low-frequency components could be different inside each tissue ($I_{A\to B}(\omega_L) << I_{B\to A}(\omega_L)$), giving the impression of some sites where the electric current is either created or annihilated. **B.** The schematic illustration of the second scenario for the CSD unbalance. The general cause-effect flow in the electrophysiological forward problem when ionic diffusion mechanisms are included. Notation: **Causes** - grey circles, **Effect** - white circles.

**Table I.** The main characteristics of the three inverse solutions used in this paper to evaluate the impact of multipolar current sources on EEG data.

**Table II.** The goodness-of-fit for each inverse solution and the estimation errors in the linear regression analysis. The estimation errors in the linear regression analysis were separated in those resulting from the use of the three multipolar regressors and those obtained using a leave one out strategy. The errors in the first, second and third columns for the leave one out strategy were obtained by excluding from the linear regression model the monopolar, dipolar and quadrupolar regressors, respectively.

# Table I

| Inverse Solution | Source Model | Constraints |
|---|---|---|
| Equivalent Dipole | *dipole* | *orientation/location "fixed"* |
| LORETA | *dipole* | *spatial smoothing* |

# Table II

| Stimulus frequency | goodness-of-fit | Linear Regression Analysis | | | |
|---|---|---|---|---|---|
| | | Three multipoles | Leave One Out | | |
| | | | Monopole | Dipole | Quadrupole |
| **Equivalent Dipole** | | | | | |
| **1 Hz** | **61%** | 0.17±0.08 | 0.23±0.07 | 0.19±0.08 | 0.20±0.08 |
| **3 Hz** | **75%** | 0.11±0.08 | 0.17±0.09 | 0.13±0.08 | 0.13±0.07 |
| **LORETA** | | | | | |
| **1 Hz** | **65%** | 0.17±0.06 | 0.25±0.10 | 0.19±0.05 | 0.20±0.05 |
| **3 Hz** | **83%** | 0.11±0.07 | 0.19±0.10 | 0.13±0.08 | 0.13±0.06 |

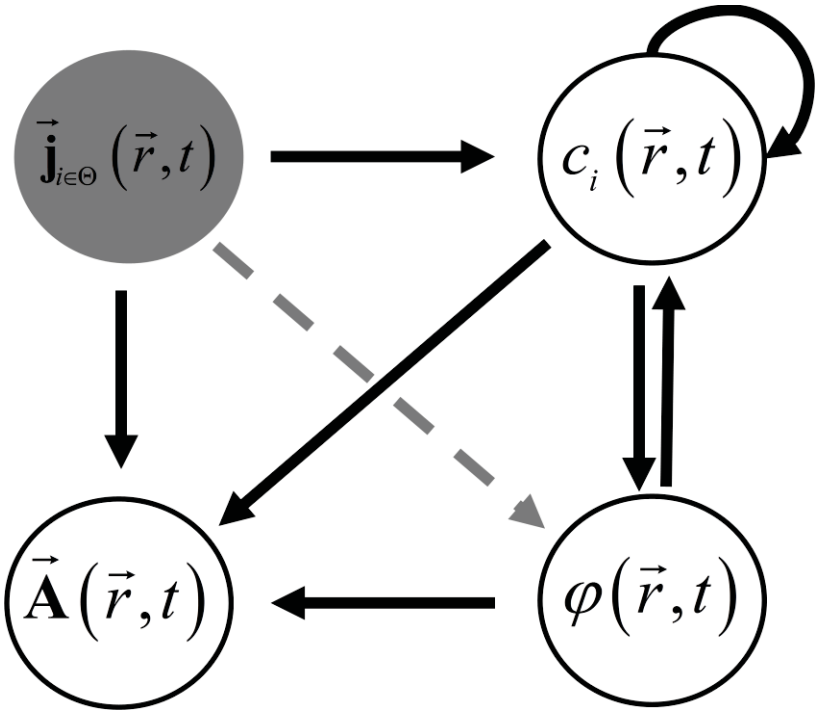
$\vec{\mathbf{j}}_{i\in\Theta}\left(\vec{r},t\right)$
$c_i\left(\vec{r},t\right)$
$\vec{\mathbf{A}}\left(\vec{r},t\right)$
$\varphi\left(\vec{r},t\right)$

**Figure I-B**

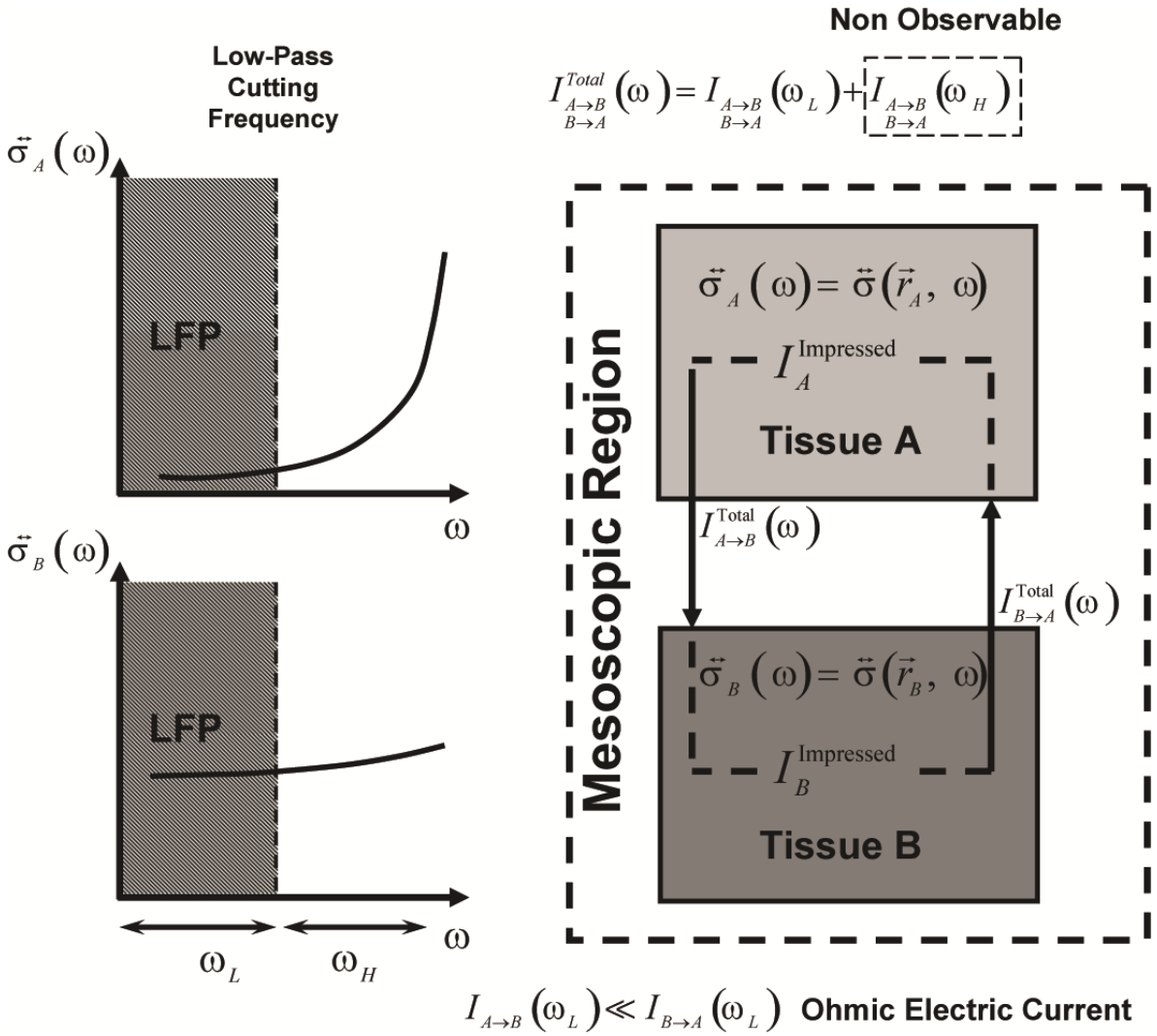
Non Observable
$I^{Total}_{\substack{A\to B\\B\to A}}(\omega)=I_{\substack{A\to B\\B\to A}}(\omega_L)+I_{\substack{A\to B\\B\to A}}(\omega_H)$
Low-Pass
Cutting
Frequency
$\vec{\vec{\sigma}}_A(\omega)$
LFP
$\omega$
$\vec{\vec{\sigma}}_B(\omega)$
LFP
$\omega$
$\omega_L$
$\omega_H$
Mesoscopic Region
$\vec{\vec{\sigma}}_A(\omega)=\vec{\vec{\sigma}}(\vec{r}_A,\omega)$
$I_A^{Impressed}$
Tissue A
$I^{Total}_{A\to B}(\omega)$
$I^{Total}_{B\to A}(\omega)$
$\vec{\vec{\sigma}}_B(\omega)=\vec{\vec{\sigma}}(\vec{r}_B,\omega)$
$I_B^{Impressed}$
Tissue B
$I_{A\to B}(\omega_L)\ll I_{B\to A}(\omega_L)$ Ohmic Electric Current

**Figure I-A**

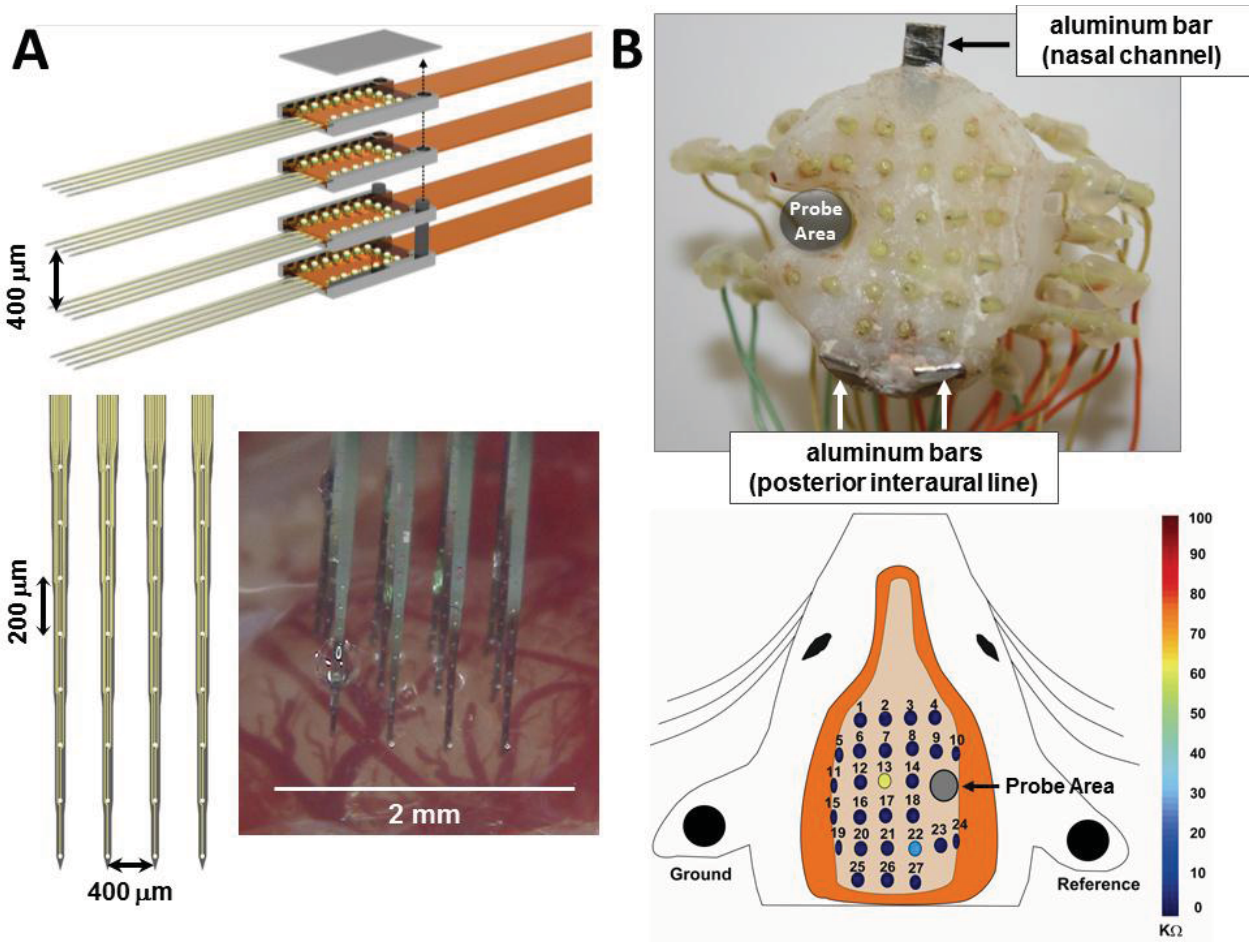
A
400 µm
200 µm
400 µm
2 mm
B
aluminum bar
(nasal channel)
Probe
Area
aluminum bars
(posterior interaural line)
Probe Area
Ground
Reference
100
90
80
70
60
50
40
30
20
10
0
KΩ

**Figure 1**

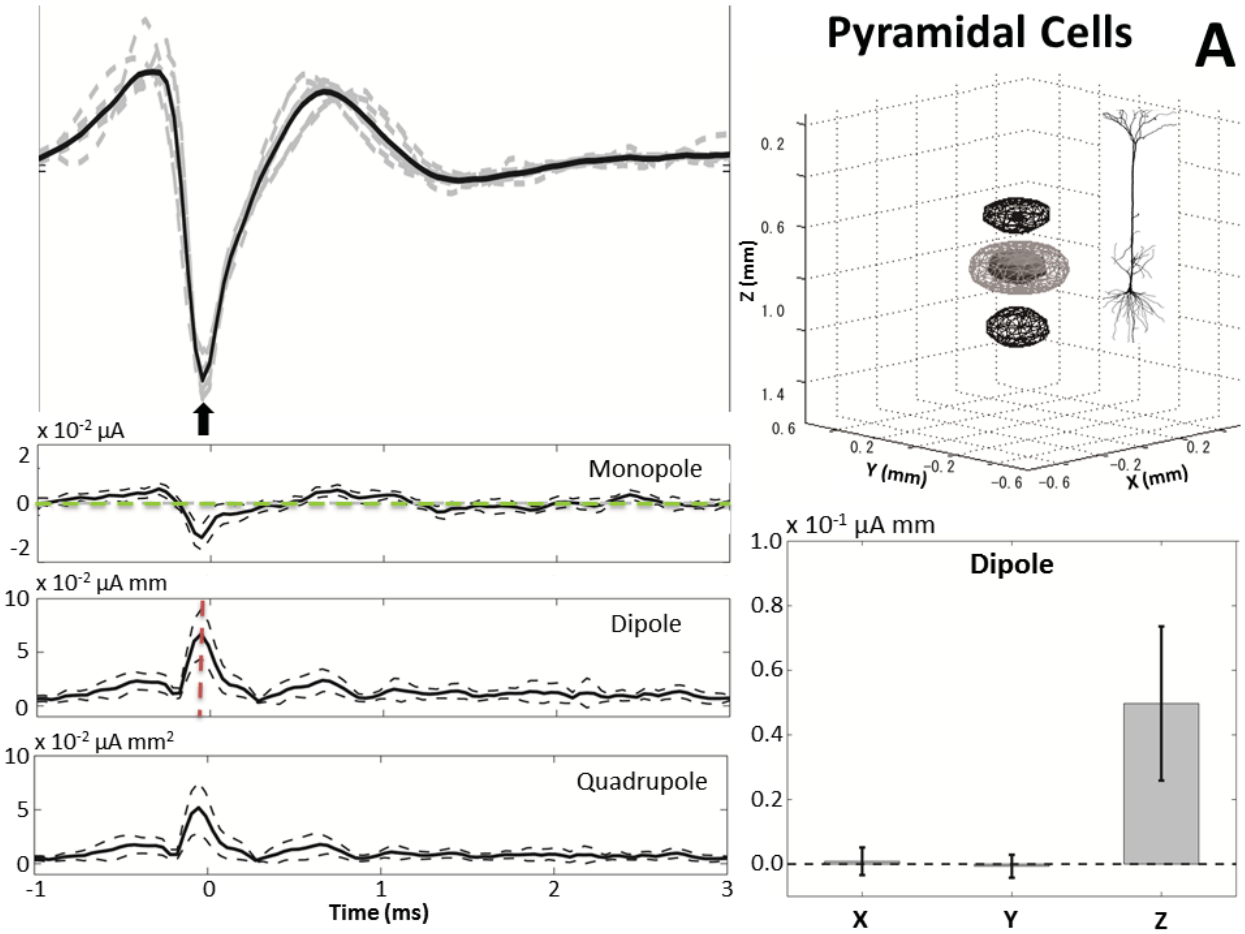
Pyramidal Cells
A
x 10-2 µA
Monopole
x 10-2 µA mm
Dipole
x 10-2 µA mm2
Quadrupole
Time (ms)
Z (mm)
Y (mm)
X (mm)
x 10-1 µA mm
Dipole
X
Y
Z

**Figure 2A**

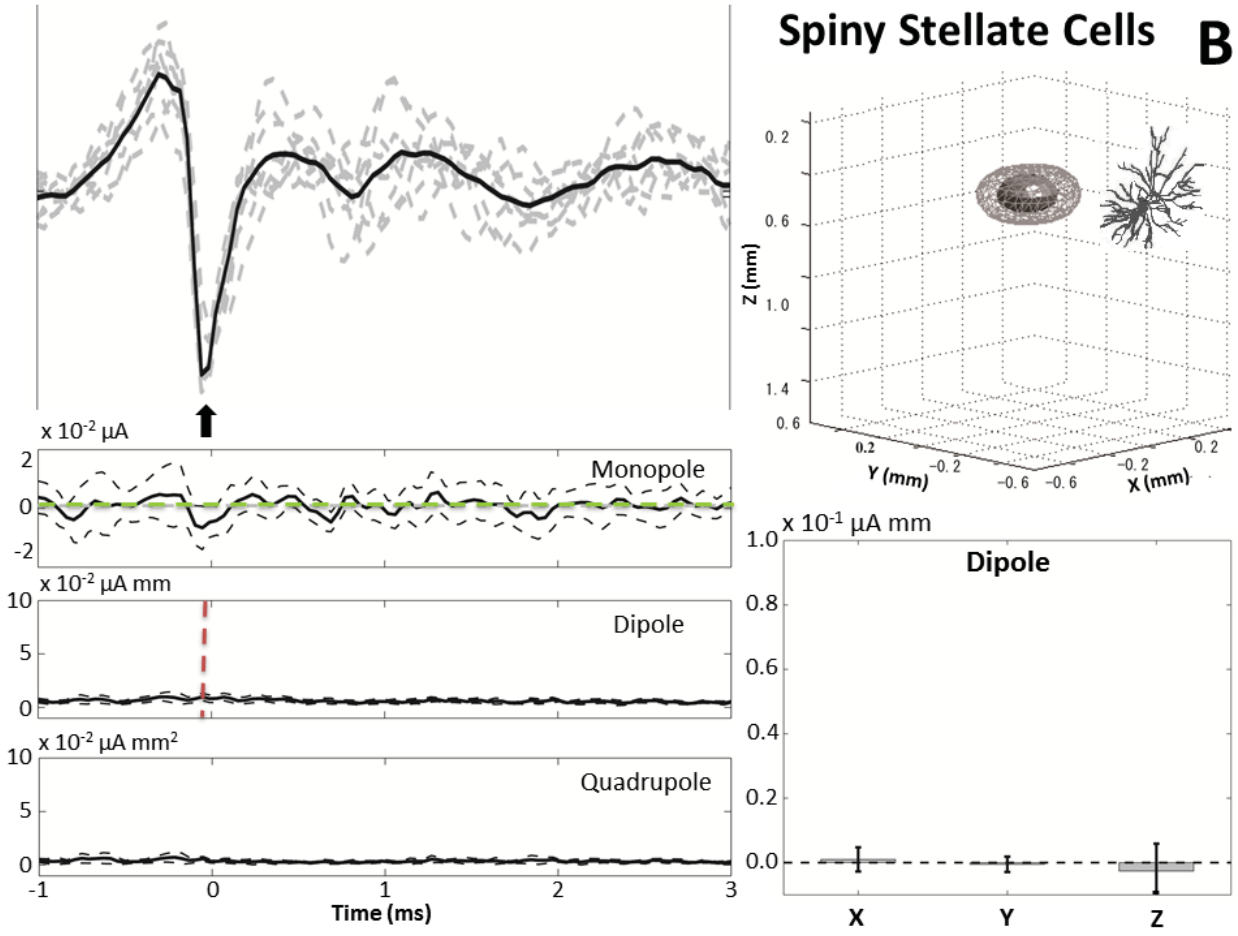
Spiny Stellate Cells
B
x 10-2 µA
Monopole
x 10-2 µA mm
Dipole
x 10-2 µA mm2
Quadrupole
Time (ms)
Z (mm)
Y (mm)
X (mm)
x 10-1 µA mm
Dipole
X
Y
Z

**Figure 2B**

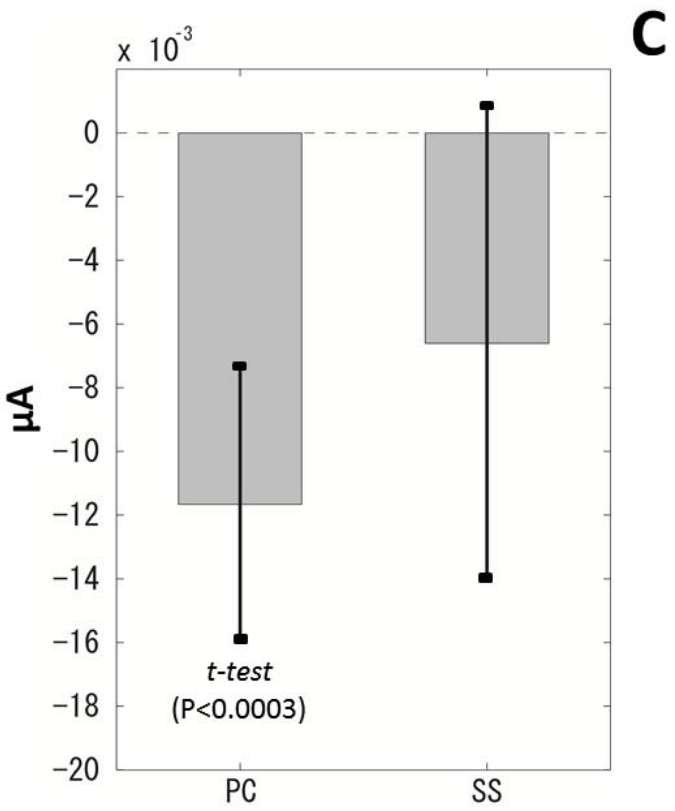


**Figure 2C**

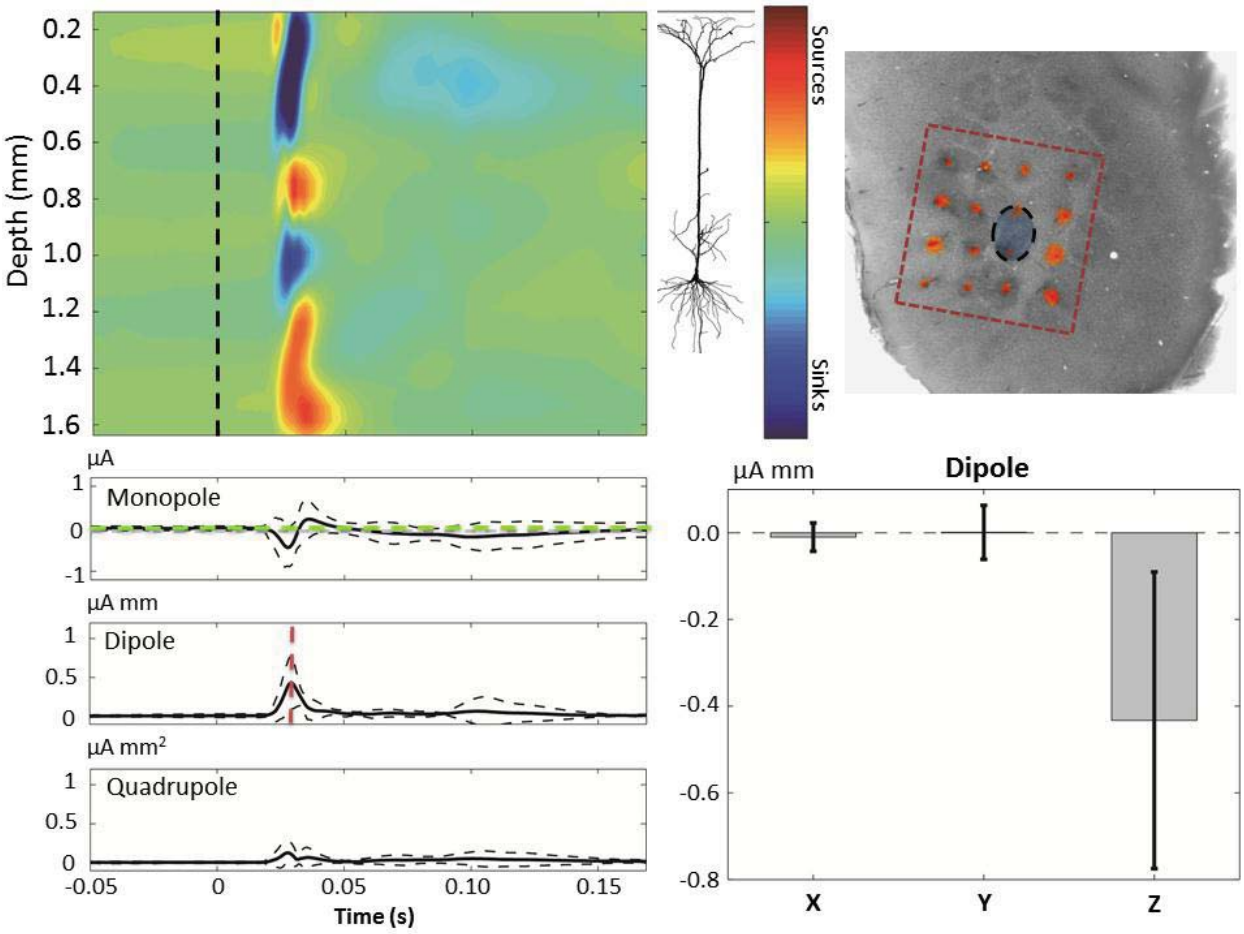
Depth (mm)
0.2
0.4
0.6
0.8
1.0
1.2
1.4
1.6
Sources
Sinks
µA
Monopole
µA mm
Dipole
µA mm²
Quadrupole
Time (s)
-0.05
0
0.05
0.10
0.15
µA mm
Dipole
X
Y
Z

**Figure 3**

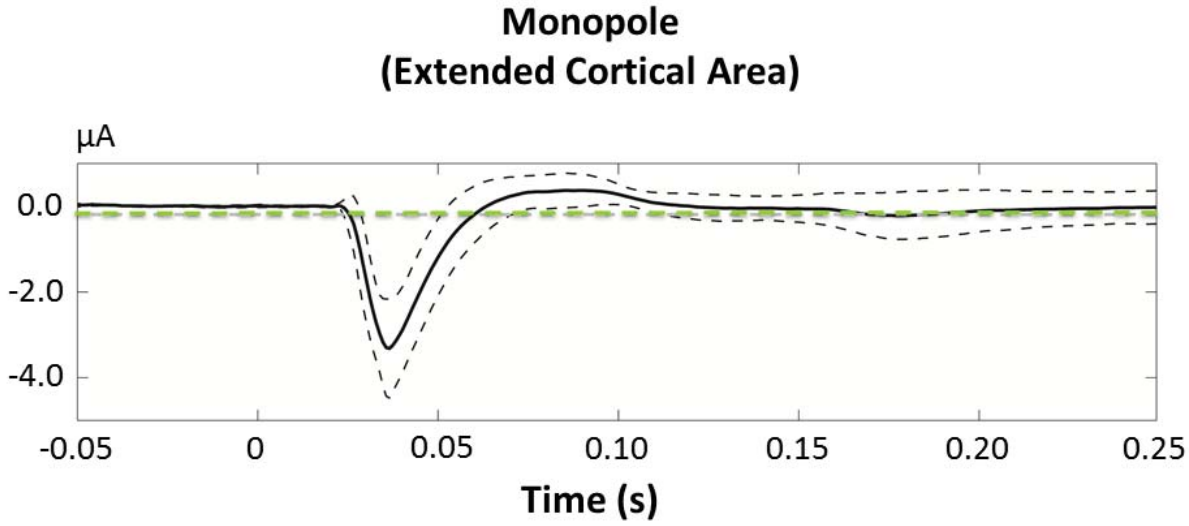
Monopole
(Extended Cortical Area)
µA
0.0
-2.0
-4.0
-0.05
0
0.05
0.10
0.15
0.20
0.25
Time (s)

**Figure 4**

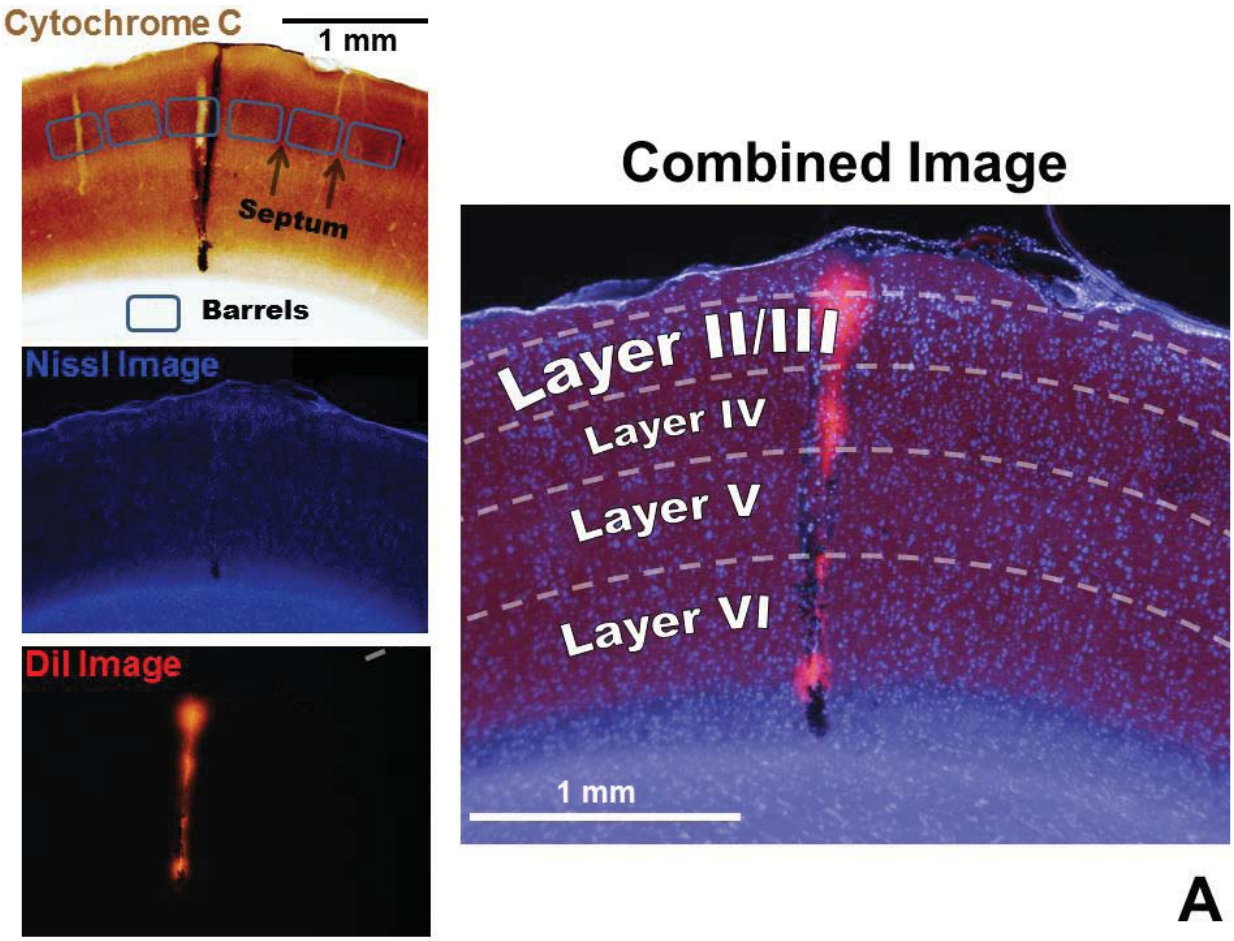
Cytochrome C
1 mm
Septum
Barrels
Nissl Image
DiI Image
Combined Image
Layer II/III
Layer IV
Layer V
Layer VI
1 mm
A

Figure 5A

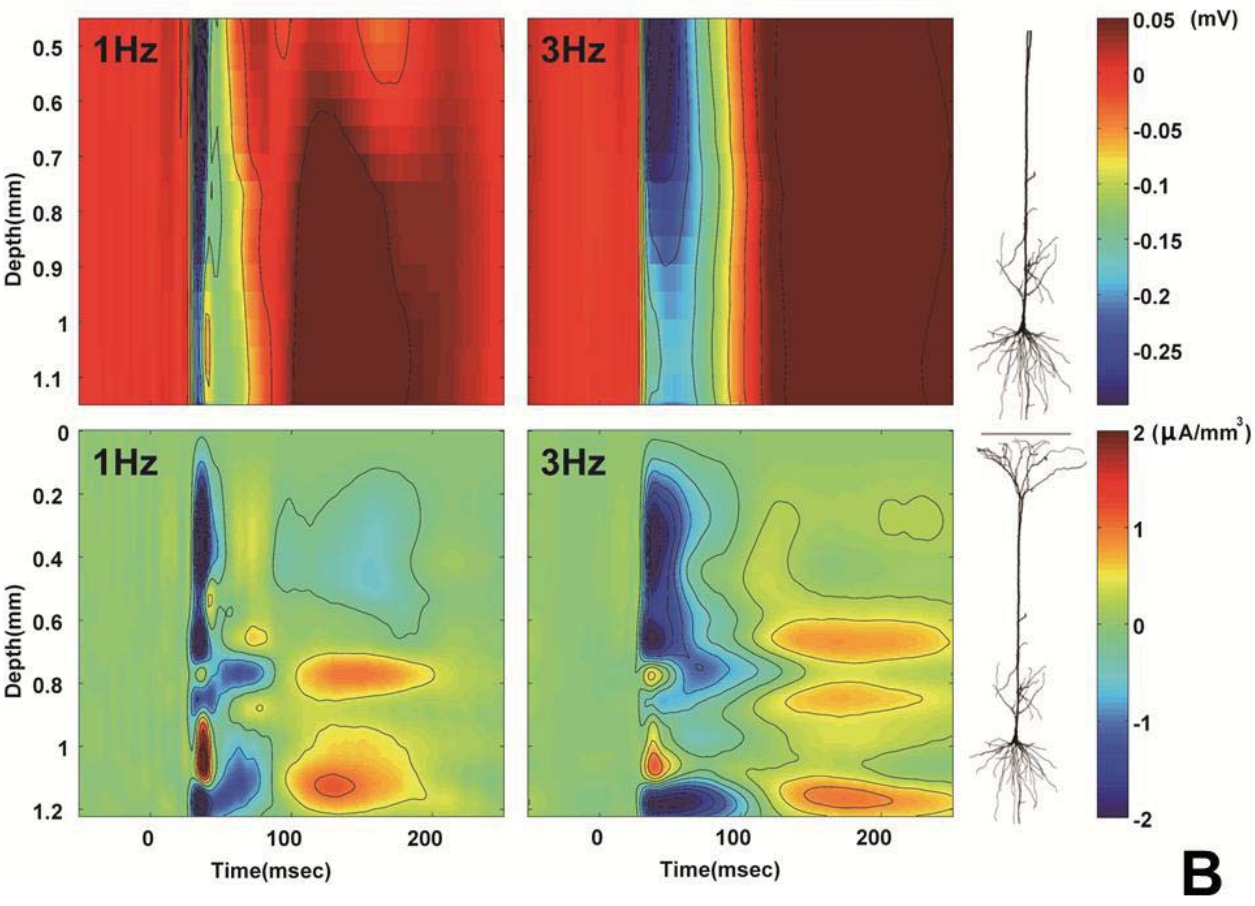
1Hz
3Hz
Depth(mm)
0.5
0.6
0.7
0.8
0.9
1
1.1
0.05 (mV)
0
-0.05
-0.1
-0.15
-0.2
-0.25
1Hz
3Hz
Depth(mm)
0
0.2
0.4
0.6
0.8
1
1.2
2 (μA/mm3)
1
0
-1
-2
0
100
200
Time(msec)
0
100
200
Time(msec)
B

**Figure 5B**

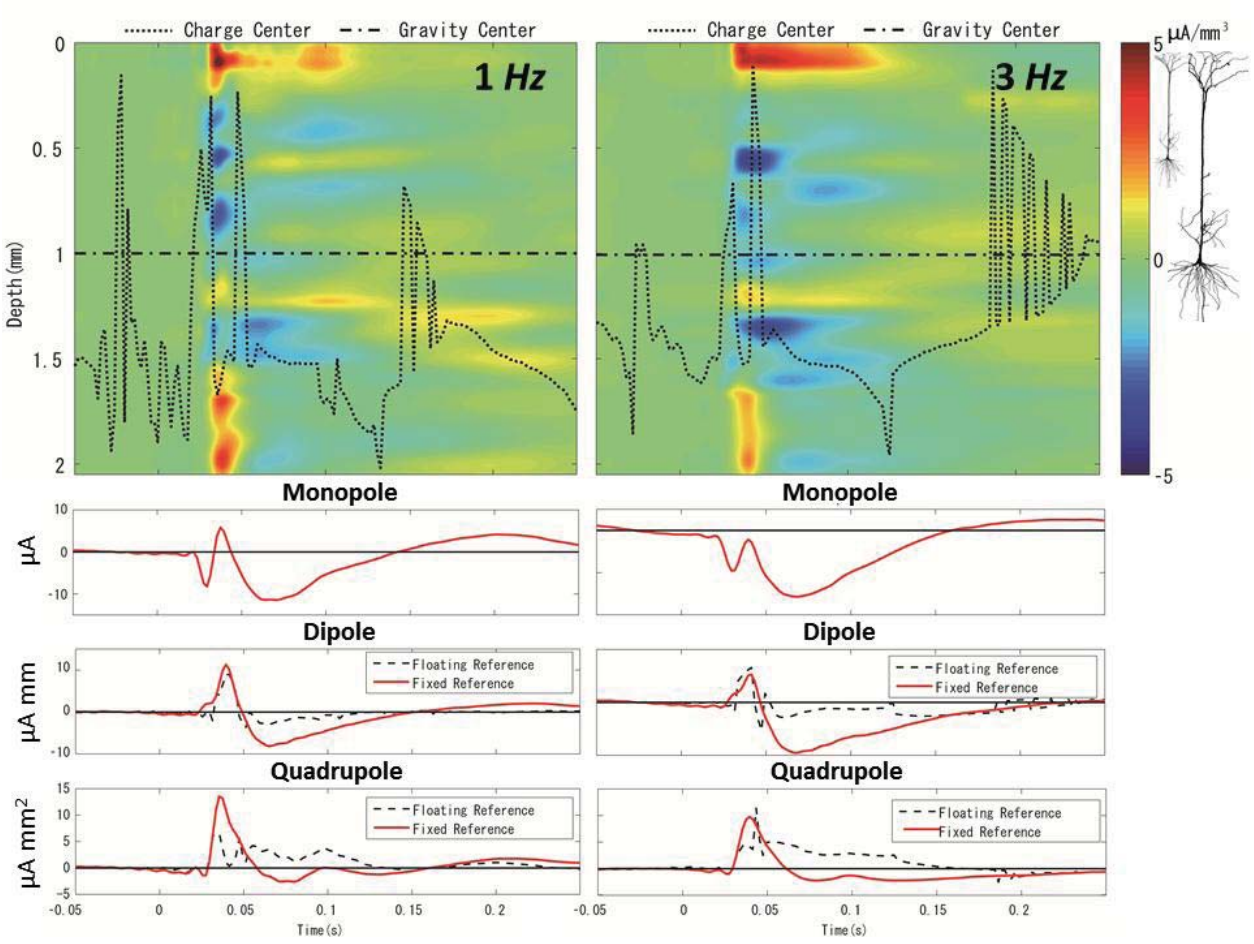
Charge Center
Gravity Center
1 Hz
3 Hz
Depth (mm)
μA/mm³
Monopole
Dipole
Quadrupole
μA
μA mm
μA mm²
Floating Reference
Fixed Reference
Time (s)

**Figure 6**

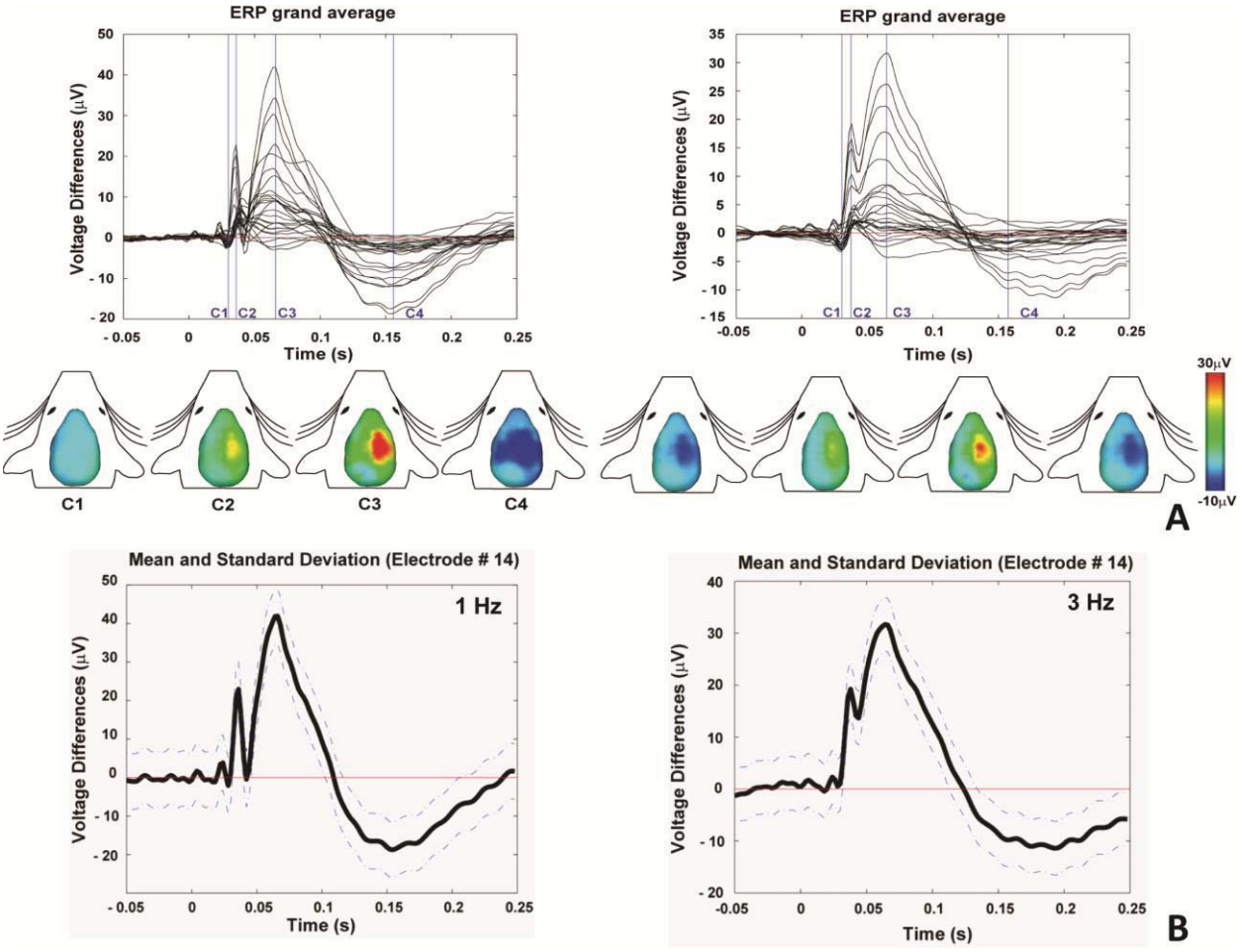
ERP grand average
Voltage Differences (μV)
Time (s)
C1
C2
C3
C4
ERP grand average
Voltage Differences (μV)
Time (s)
C1
C2
C3
C4
30μV
-10μV
A
Mean and Standard Deviation (Electrode # 14)
1 Hz
Voltage Differences (μV)
Time (s)
Mean and Standard Deviation (Electrode # 14)
3 Hz
Voltage Differences (μV)
Time (s)
B

**Figure 7**

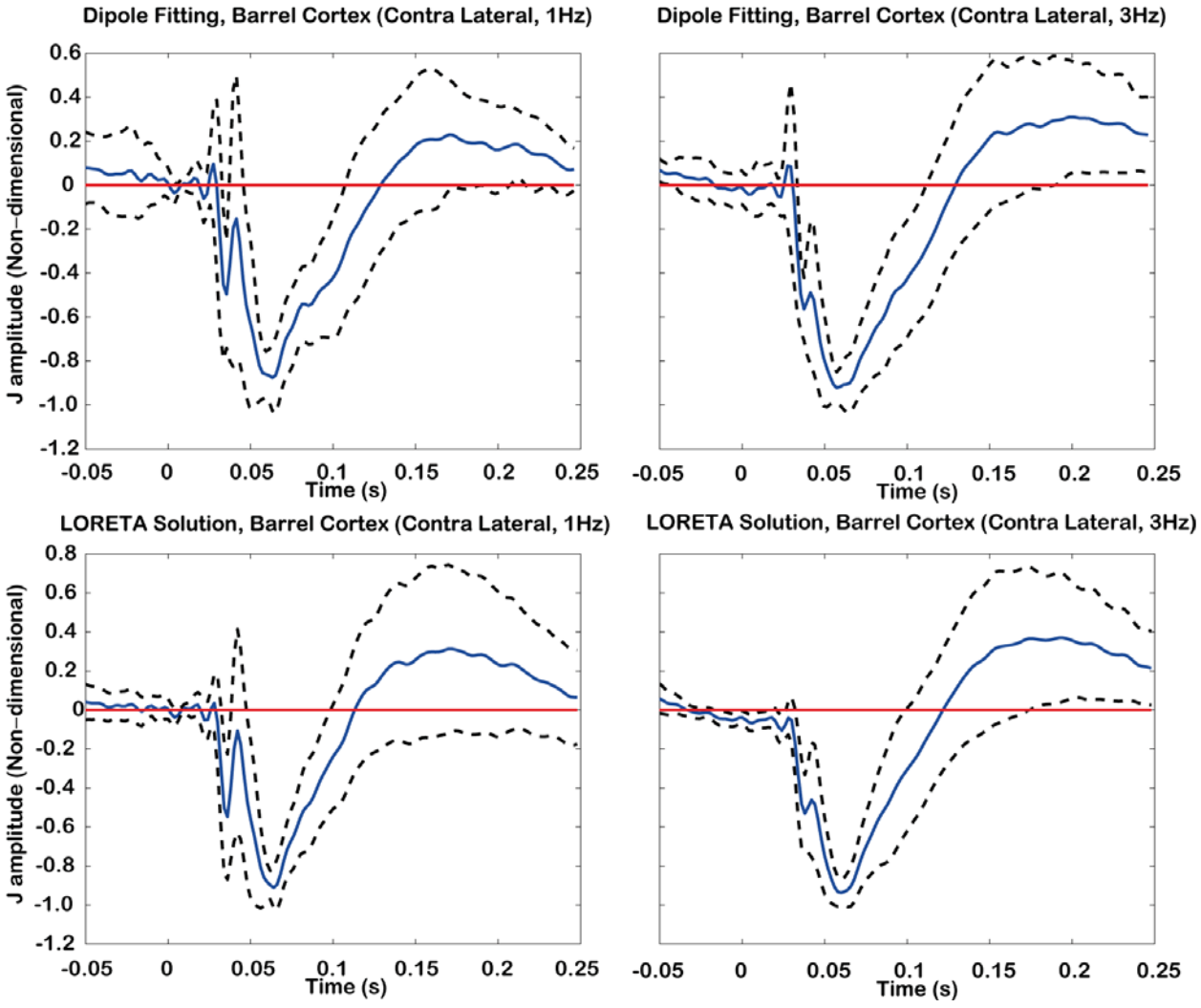
Dipole Fitting, Barrel Cortex (Contra Lateral, 1Hz)
Dipole Fitting, Barrel Cortex (Contra Lateral, 3Hz)
LORETA Solution, Barrel Cortex (Contra Lateral, 1Hz)
LORETA Solution, Barrel Cortex (Contra Lateral, 3Hz)
J amplitude (Non−dimensional)
Time (s)

**Figure 8**

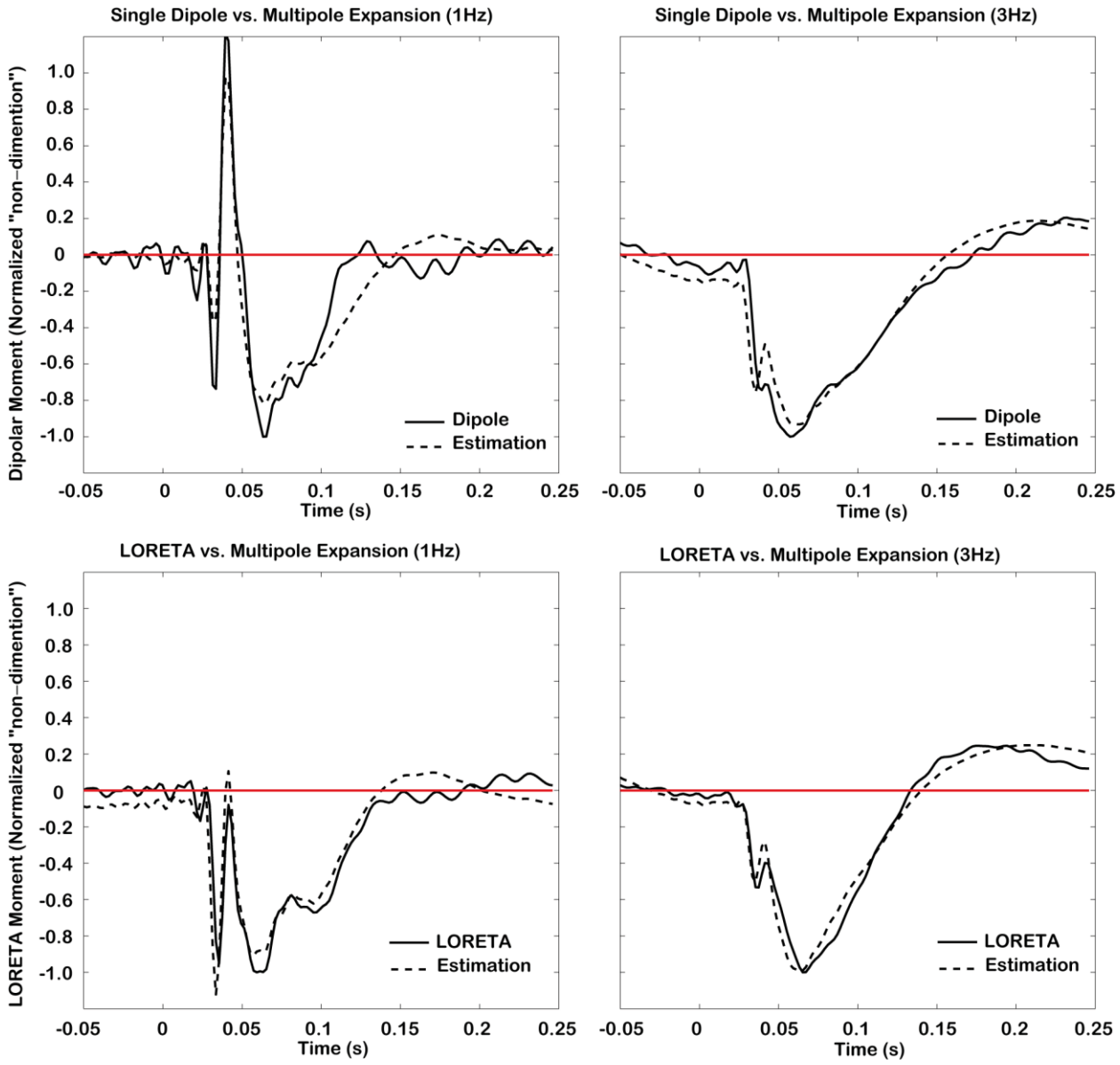
Single Dipole vs. Multipole Expansion (1Hz)
Single Dipole vs. Multipole Expansion (3Hz)
Dipolar Moment (Normalized "non−dimention")
Dipole
Estimation
Time (s)
LORETA vs. Multipole Expansion (1Hz)
LORETA vs. Multipole Expansion (3Hz)
LORETA Moment (Normalized "non−dimention")
LORETA
Estimation

**Figure 9**

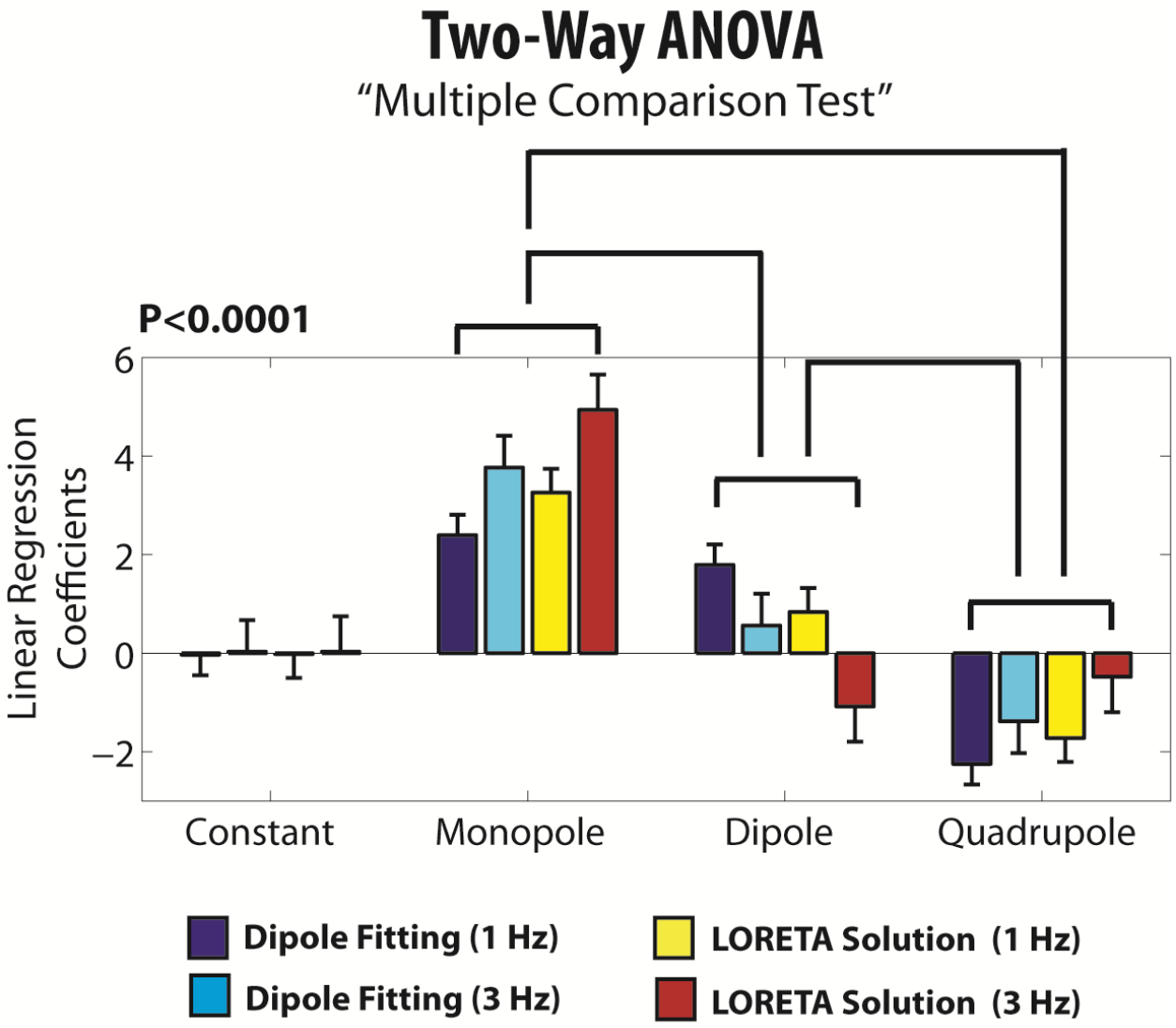
Two-Way ANOVA
"Multiple Comparison Test"
P<0.0001
Linear Regression Coefficients
6
4
2
0
−2
Constant
Monopole
Dipole
Quadrupole
Dipole Fitting (1 Hz)
Dipole Fitting (3 Hz)
LORETA Solution (1 Hz)
LORETA Solution (3 Hz)

**Figure 10**